Article

Cell Reports

An integrated genomic approach to dissect the genetic landscape regulating the cell-to-cell transfer of α-synuclein

Graphical abstract

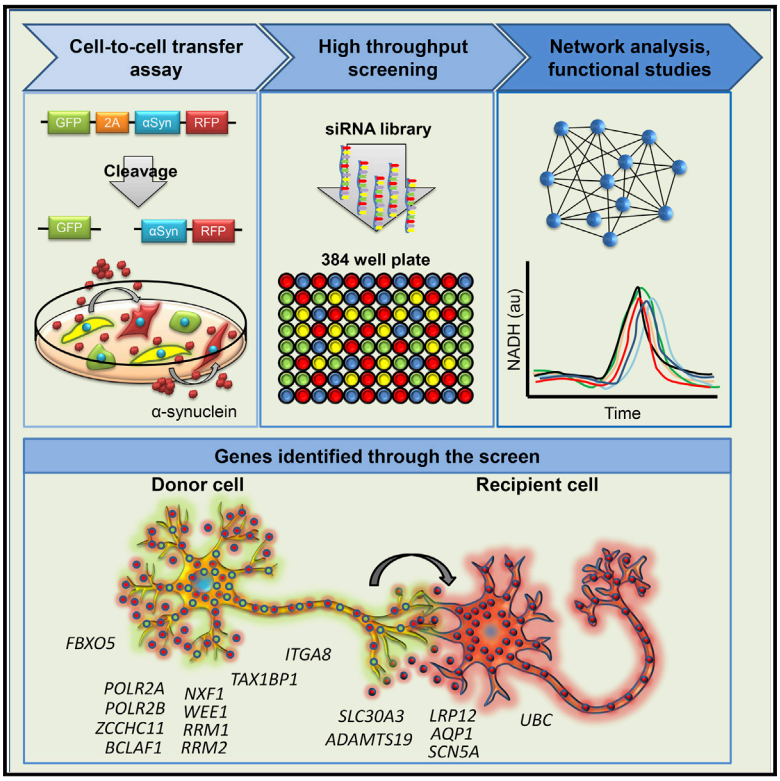

Highlights

- 38 genes regulate the cell-to-cell transfer of α-synuclein
- Those genes participate in the same networks as known Parkinson's disease (PD) genes
- Knockdown of selected genes affects mitochondrial $\Delta\Psi m$ similarly to recessive PD genes
- The "prionoid" hypothesis likely has an important role in the pathogenesis of PD

Authors

Eleanna Kara, Alessandro Crimi, Anne Wiedmer, ..., John Hardy, Bradley T. Hyman, Adriano Aguzzi

Correspondence

adriano.aguzzi@usz.ch

In brief

Kara et al. undertook a high-throughput screen that identified 38 genes that regulate the cell-to-cell transfer of α-synuclein. Those genes participate in the same networks as known Parkinson's disease Mendelian and risk genes. This work provides a framework for a gene-discovery strategy in complex diseases.

Kara et al., 2021, Cell Reports *35*, 109189
June 8, 2021
https://doi.org/10.1016/j.celrep.2021.109189

CellPress

Cell Reports

CellPress
OPEN ACCESS

Article

An integrated genomic approach to dissect the genetic landscape regulating the cell-to-cell transfer of α-synuclein

Eleanna Kara,[1,2] Alessandro Crimi,[1,21] Anne Wiedmer,[1,21] Marc Emmenegger,[1,21] Claudia Manzoni,[3,4] Sara Bandres-Ciga,[5] Karishma D'Sa,[6,7,8] Regina H. Reynolds,[8,9] Juan A. Botía,[2,10] Marco Losa,[1] Veronika Lysenko,[11] Manfredi Carta,[1] Daniel Heinzer,[1] Merve Avar,[1] Andra Chincisan,[1] Cornelis Blauwendraat,[5] Sonia García-Ruiz,[8,9] Daniel Pease,[1] Lorene Mottier,[1] Alessandra Carrella,[1] Dezirae Beck-Schneider,[1] Andreia D. Magalhães,[1] Caroline Aemisegger,[12] Alexandre P.A. Theocharides,[11] Zhanyun Fan,[13] Jordan D. Marks,[13,14] Sarah C. Hopp,[15,16] Andrey Y. Abramov,[7] Patrick A. Lewis,[2,4,17] Mina Ryten,[8,9] John Hardy,[2,18,19,20] Bradley T. Hyman,[13] and Adriano Aguzzi[1,22,*]

[1]Institute of Neuropathology, University of Zurich and University Hospital Zurich, Zurich 8091, Switzerland
[2]Department of Neurodegenerative disease, University College London, London WC1N 3BG, UK
[3]Department of Pharmacology, University College London School of Pharmacy, London WC1N 1AX, UK
[4]School of Pharmacy, University of Reading, Reading RG6 6AP, UK
[5]Laboratory of Neurogenetics, National Institutes of Health, Bethesda, MD 20814, USA
[6]The Francis Crick Institute, 1 Midland Road, London NW1 1AT, UK
[7]Department of Clinical and Movement Neurosciences, UCL Queen Square Institute of Neurology, London WC1N 3BG, UK
[8]Department of Genetics and Genomic Medicine, Great Ormond Street Institute of Child Health, University College London, London, UK
[9]NIHR Great Ormond Street Hospital Biomedical Research Centre, University College London, London, UK
[10]Departamento de Ingeniería de la Información y las Comunicaciones, Universidad de Murcia, Murcia 30100, Spain
[11]Department of Medical Oncology and Hematology, University Hospital Zurich and University of Zurich, Zurich 8091, Switzerland
[12]Center for Microscopy and Image Analysis, University of Zurich, Zurich 8057, Switzerland
[13]Department of Neurology, Massachusetts General Hospital and Harvard Medical School, Boston, MA 02129, USA
[14]Mayo Clinic Alix School of Medicine, Mayo Clinic, Rochester, MN 55905, USA
[15]Department of Pharmacology, UT Health San Antonio, San Antonio, TX 78229, USA
[16]Glenn Biggs Institute for Alzheimer's and Neurodegenerative Diseases, UT Health San Antonio, San Antonio, TX 78229, USA
[17]Department of Comparative Biomedical Sciences, Royal Veterinary College, London NW1 0TU, UK
[18]UK Dementia Research Institute, University College London, London WC1N 3BG, UK
[19]Reta Lila Weston Institute, UCL Queen Square Institute of Neurology, 1 Wakefield Street, London WC1N 1PJ, UK
[20]Institute for Advanced Study, the Hong Kong University of Science and Technology, Hong Kong SAR, China
[21]These authors contributed equally
[22]Lead contact
*Correspondence: adriano.aguzzi@usz.ch
https://doi.org/10.1016/j.celrep.2021.109189

SUMMARY

Neuropathological and experimental evidence suggests that the cell-to-cell transfer of α-synuclein has an important role in the pathogenesis of Parkinson's disease (PD). However, the mechanism underlying this phenomenon is not fully understood. We undertook a small interfering RNA (siRNA), genome-wide screen to identify genes regulating the cell-to-cell transfer of α-synuclein. A genetically encoded reporter, GFP-2A-αSynuclein-RFP, suitable for separating donor and recipient cells, was transiently transfected into HEK cells stably overexpressing α-synuclein. We find that 38 genes regulate the transfer of α-synuclein-RFP, one of which is *ITGA8*, a candidate gene identified through a recent PD genome-wide association study (GWAS). Weighted gene co-expression network analysis (WGCNA) and weighted protein-protein network interaction analysis (WPPNIA) show that those hits cluster in networks that include known PD genes more frequently than expected by random chance. The findings expand our understanding of the mechanism of α-synuclein spread.

INTRODUCTION

The cell-to-cell transfer of α-synuclein (αSyn) is thought to be an important event in the pathogenesis of Parkinson's disease (PD). The first evidence suggesting a role of this phenomenon came from post-mortem analyses of brains from patients with PD who had received neuronal grafts in the midbrain and showed that those healthy neurons had developed Lewy bodies (Kordower et al., 2008; Li et al., 2008). In addition, patients with PD develop αSyn pathology

in the brain that follows a consistent pattern, starting from the brain stem and olfactory bulb and moving up to the cortex (Braak et al., 2003), which is consistent with the spread of an "agent," which is thought to be misfolded αSyn. Those observations have been supported by experimental evidence generated through studies on mouse models and tissue culture systems (Luk et al., 2009, 2012, 2016; Rey et al., 2018; Thakur et al., 2017; Volpicelli-Daley et al., 2011). However, the importance of this phenomenon in the pathogenesis of PD remains controversial. A proportion of PD cases do not follow the Braak staging, and the severity of the clinical presentation often does not correlate with the Braak stage (Surmeier et al., 2017). Therefore, a suggested alternative model is the selective-vulnerability hypothesis, according to which the progressive development of pathology is not because of the spread of a pathogenic species of αSyn but because of the differential vulnerability of various brain regions to the disease process (Alegre-Abarrategui et al., 2019; Fu et al., 2018; Hardy, 2016). Additionally, the genetic underpinnings and mechanisms underlying the cell-to-cell transfer of αSyn and how those relate to known genetic causes of PD are not understood.

To address those questions, we performed a high-throughput, small interfering RNA (siRNA) genome-wide screen to find genes regulating the transfer of αSyn. Given the uncertainty regarding the nature of the transferred species of αSyn, we used a genetically encoded reporter to identify the cells that received the transferred αSyn, which does not make any assumptions regarding the aggregation state of the transferred protein. The screen identified 38 genes regulating this process, several of which have been previously linked into the pathogenesis of PD. Those findings provide insight into the mechanisms regulating the cell-to-cell transfer of αSyn.

RESULTS

Development of an assay to study the cell-to-cell transfer of αSyn

To study the cell-to-cell transfer of αSyn, we used a GFP-2A-αSynuclein-RFP reporter (Wegmann et al., 2015). As a model system, we used a HEK QBI cell line stably overexpressing human wild-type (WT) αSyn (HEK-αSyn line) (Luk et al., 2009). The translated protein is cleaved at the 2A peptide into two proteins, GFP and αSyn-RFP. αSyn-RFP then transfers to neighboring cells without concomitant transfer of GFP. Donor and recipient cells can, therefore, be identified by their colors: the cells expressing αSyn through transfection are positive for GFP and RFP, whereas the cells that receive αSyn through transfer are positive for RFP only (Figure 1A). We observed that transferred αSyn formed punctate cytoplasmic structures, primarily within the cellular processes (Figure 1B).

We isolated through fluorescence-activated cell sorting (FACS) the population that expressed αSyn-RFP through transfection (RFP^+GFP^+) and the population that had taken up αSyn-RFP through transfer (RFP^+GFP^-) 5 days after transfection (Figure S1A) and analyzed them through western blot. Recipient cells contained only αSyn-RFP (expected molecular weight 41 kDa) and untagged endogenous αSyn, whereas donor cells additionally expressed some uncleaved GFP-2A-αSyn-RFP protein (expected molecular weight 68 kDa) (Figure 1C). The absence of the αSyn-RFP transcript in the recipient cells was confirmed by qPCR (Figure S1B).

We first characterized the assay using transient transfections in tissue culture, followed by flow cytometry. In a time-course experiment, we found an increase over time of the number of RFP^+GFP^- cells that had received αSyn-RFP through transfer (Figures 1D and 1E). As a negative control, we used a construct encoding GFP-2A-RFP and found that, although RFP was capable of transferring between cells, αSyn-RFP transferred at a significantly higher ratio in the HEK-αSyn line (Figure 1F). No difference between the transfer ratio of RFP and αSyn-RFP was observed in other cell lines (Figures S1C–S1G), none of which expressed endogenous αSyn (Figure S1H). Those results suggest that endogenous expression of αSyn facilitates the transfer of the αSyn-RFP fusion protein, which is consistent with the permissive-templating hypothesis (Hardy, 2005).

Because αSyn in the recipient cells did not spread diffusely within the cytoplasm and nucleus, we confirmed that the recipient RFP^+GFP^- events detected on flow cytometry were intact cells and not debris; 98% of RFP^+GFP^- cells that were analyzed by flow cytometry were found to contain a nucleus, as determined by positive Hoechst staining, a percentage comparable to that of the other populations (Figure 1G). In addition, we incubated the cells with a live/dead dye and found that all 4 populations had a death ratio of less than 4% (Figure 1H).

A genome-wide siRNA screen for the identification of genetic modifiers of αSyn spread

We first determined the optimal concentration and incubation time of the siRNA. As a positive control, we used 3 pooled siRNAs against αSyn, with a final concentration of 5 nM, and co-transfected them with the GFP-2A-αSyn-RFP construct. Separately, we also co-transfected the construct with Cy5-tagged siRNA. Flow cytometry that was performed 5 days later showed that the transfection efficiency of the siRNAs was 93% ± 16% (Figure 2A), with an 81% ± 12% reduction in αSyn-RFP mean fluorescence intensity (MFI) after treatment with the anti-αSyn siRNA pool (Figure 2B).

We miniaturized the assay into a 384-well-plate format that was suitable for imaging (Figure S2A). For quality control, we used the plate heatmaps, z′-factor, and strictly standardized mean difference (SSMD) (Zhang, 2008) (Figure S2B). The average z′-factor from the entire screen was 0.36, which is within the acceptable range (Figure 2E). The SSMD was also acceptable for most of the plates (Figure S2C). The histograms of the positive (*SNCA* siRNAs) and negative (scrambled siRNAs) controls confirmed a good separation (Figure 2F).

The replicability between technical duplicates was assessed by the Bland-Altman and Deming regression tests. The bias metric calculated through the Bland-Altman test was 0.1 (Figure 2C). The slope calculated through the Deming regression was significantly different than zero and approached 1, corresponding to a 45° angle, also supporting concordance between technical replicates (Figure 2D). The siRNAs were ranked by p value (Figures 2G and S2D–S2F). *SNCA* was identified as the top hit of the screen (Figure S2G).

CellPress
OPEN ACCESS

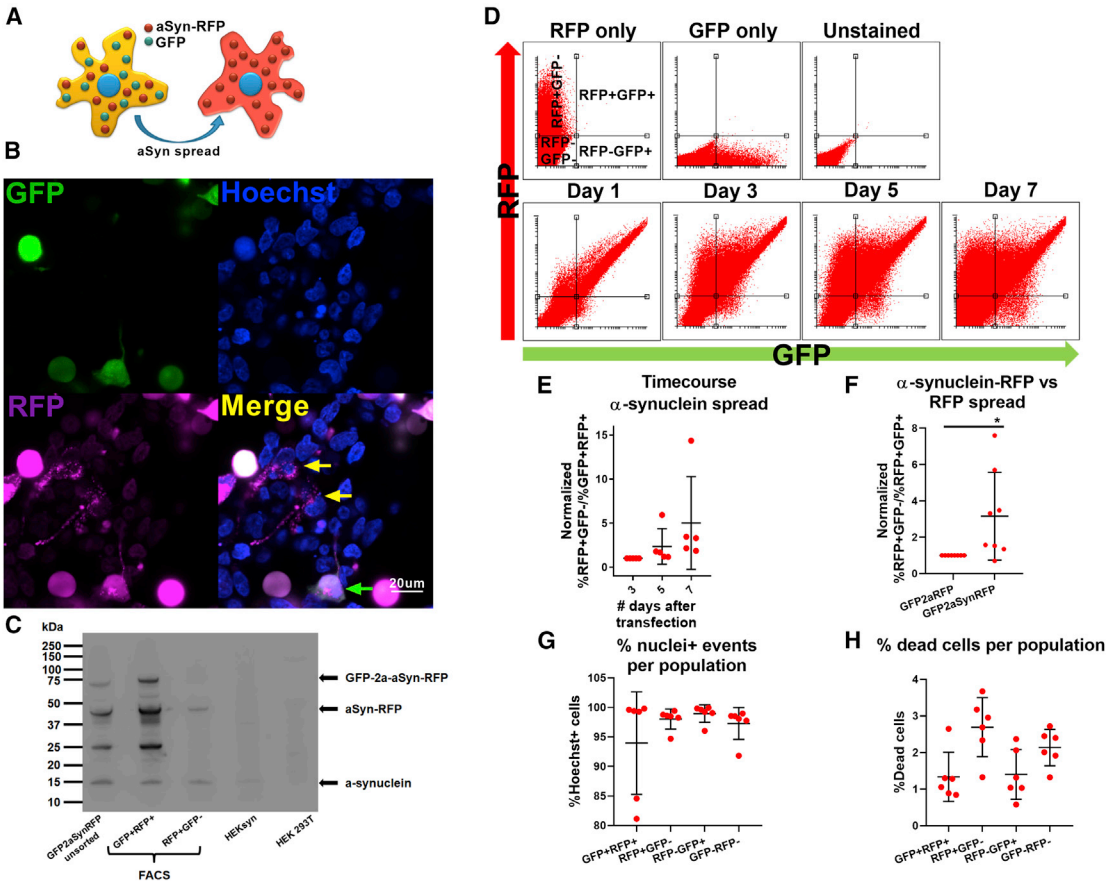

Figure 1. Development of an assay to study the cell-to-cell transfer of αSyn

(A) Cartoon depicting the rationale behind the αSyn transfer assay used, based on the GFP-2A-αSyn-RFP construct.

(B) Confocal images showing one HEK-αSyn cell that was transfected with the GFP-2A-αSyn-RFP construct and is double positive for GFP and RFP (green arrow), and 2 cells that have received αSyn-RFP through transfer and are positive for RFP but negative for GFP (yellow arrows). Scale bar, 20 μm.

(C) Western blot experiment on bulk HEK-αSyn cells transfected with the GFP-2A-αSyn-RFP construct. FACS-sorted RFP^+GFP^+ and RFP^+GFP^- cells were also included. The membrane was probed with an anti-αSyn antibody.

(D) Flow cytometry plots corresponding to a representative experiment from (E). Single-color controls and unstained samples are shown to demonstrate how the gates were set.

(E) Time-course experiment in which the HEK-αSyn cells were transfected with the GFP-2A-αSyn-RFP construct, followed by collection on days 3, 5, and 7 and analysis through flow cytometry. This experiment was repeated independently 5 times. Data were normalized to the samples collected 3 days after transfection. One-way ANOVA with a test for trend, $\alpha = 0.05$.

(F) The transfer propensity of αSyn-RFP was compared with that of the negative control, RFP, using the constructs GFP-2A-αSyn-RFP and GFP-2A-RFP. The αSyn-RFP fusion protein transferred from cell-to-cell significantly more than did RFP alone. One-sample t test was used for statistical analysis. *$p < 0.05$ and > 0.01. The experiment was repeated independently 8 times and normalized to the negative control (GFP-2A-RFP) before meta-analysis.

(G) Plot showing the percentage of the events within each of the 4 populations that were positive for Hoechst, indicating that they had a nucleus and were, therefore, intact cells. The experiment was repeated independently 5 times, and the data were plotted without prior normalization.

(H) Plot showing the percentage of cells that were dead, as assessed through staining with a far-red live/dead dye. The experiment was repeated independently 5 times, and the data were plotted without prior normalization.

Secondary and tertiary screens confirm the role of 38 genes in the regulation of cell-to-cell transfer of αSyn

The top 1,000 genes identified through the primary screen were subjected to a series of follow-up screens to filter out false-positive results (Figure 3A). We first completed a screen (secondary screen) on the 1,000 genes using single siRNAs per well, in technical triplicates, to assess off target effects (Figures 3B, 3C, S3A, and S3B).

The criteria that needed to be fulfilled for a gene to be carried on to the next stage were the following: (1) at least 2 of the 3 siRNAs targeting the same gene should have a p value less than 5×10^{-5} (Bonferroni corrected p value of 0.05 for 1,000 tests) and the same directionality of effect as determined by the SSMDs, or (2) 1 of the 3 siRNAs should have a p value less than 5×10^{-5}, plus all 3 different siRNAs targeting the same gene should have the same directionality of effect. In addition, the driver siRNA(s) must have the same directionality as the pooled siRNAs from the primary screen.

A total of 152 genes fulfilled these criteria and were carried forward (Table S1), along with 80 random genes and *SNCA* (Table

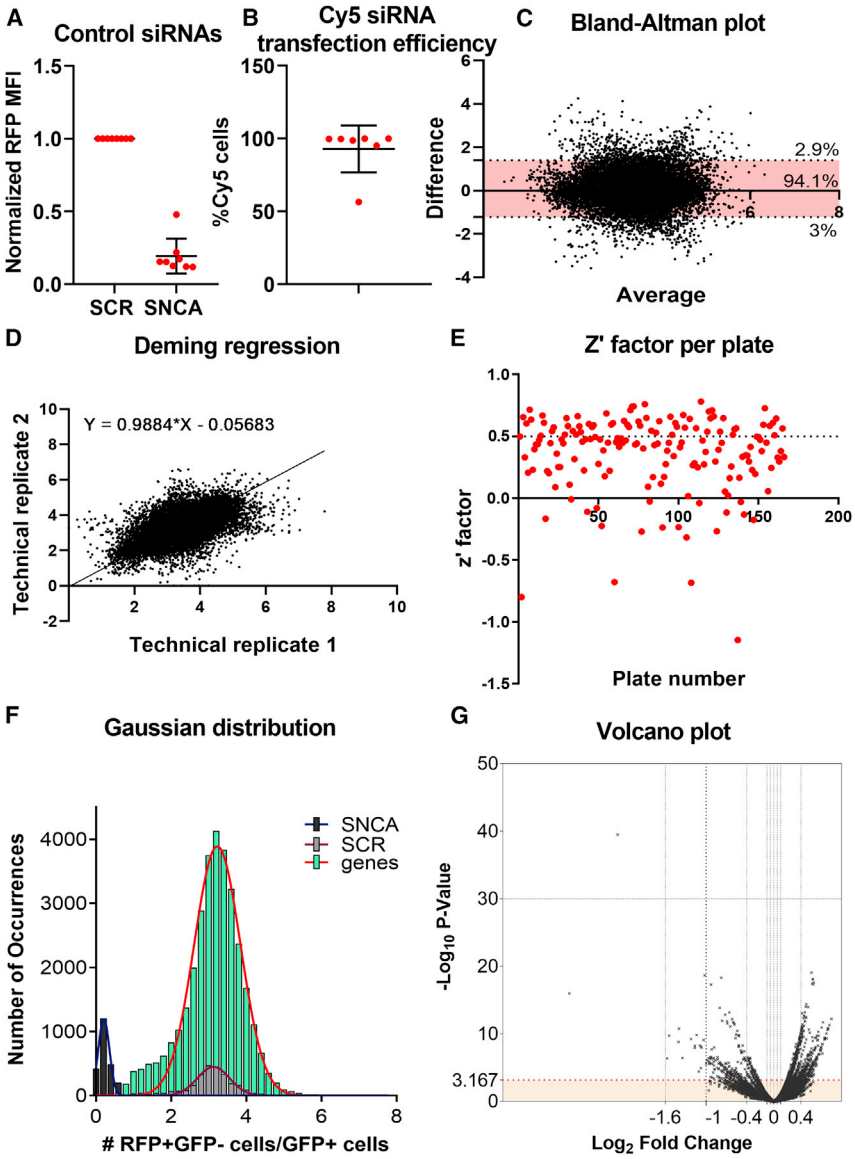

Figure 2. A genome-wide siRNA screen for the identification of genetic modifiers of αSyn spread

(A) The mean fluorescence intensity (MFI) of αSyn-RFP was quantified through flow cytometry after treatment with the positive control siRNAs against *SNCA* in comparison with the negative control of scrambled siRNA. There was an 81% ± 12% (means ± SD) reduction of the MFI after siRNA treatment. The experiment was repeated independently 5 times. The data were normalized to the negative control before collation.

(B) The transfection efficiency of the siRNAs was quantified in an experiment in which the GFP-2A-αSyn-RFP construct was co-transfected with an siRNA that was tagged with a Cy5 fluorophore. The transfection efficiency of the siRNA was 93% ± 16%. The experiment was repeated independently 5 times.

(C) Plot generated by the Bland-Altman test depicting the difference versus the average between the two technical replicates.

(D) Deming regression plot.

(E) Plot depicting the z′-factors per plate for the 166 plates included in the primary screen. Each dot represents one plate. The average z′-factor was 0.36, within the acceptable range. The cutoffs are as follows: <0, unacceptable; 0–0.5, acceptable; >0.5, excellent.

(F) Histogram of the positive (black) and negative (gray) controls and library siRNAs (green) analyzed in the entire primary screen. The separation between the positive and negative controls was good throughout the entire screen, and the library siRNAs overlapped nicely with the scrambled siRNAs.

(G) Volcano plot depicting the $\log_2$(fold change) versus $-\log_{10}$(p value) for each siRNA.

S1). The pooled library was used, and each gene was assessed in technical quadruplicates. The tertiary screen was repeated 3 times independently. For a gene to be included in the final list of hits, it had to have a p value less than 2.146×10^{-4} (Bonferroni corrected p value of 0.05 for 233 tests) in all 3 screens. The Z′-factor and SSMD were calculated per plate (Figures 3D and S3C); 44 genes were confirmed (Figure 3A). None of the 80 random genes passed the cutoffs specified above. Those results were intersected with the results from the RNA sequencing performed on the HEK-αSyn cell line, confirming a final list of 39 genes (Figure 3A) that showed a good separation from non-hits (Figures 3F–H, S3D). The Gene Ontology (GO) enrichment results for the 38 genes (excluding *SNCA*) are shown in Figure 3E. The imaging-based quantifications were confirmed (in terms of directionality of effect) through flow cytometry for 82% of hits (Figure S3E).

Because the screen was performed using a construct encoding a fusion protein αSyn-RFP, we counter-screened the hits against RFP alone. Not surprisingly, because (1) we know that a small amount of RFP alone can transfer between cells (Figure 1F), and (2) we were using a non-biased screen that detects genes that affect a process that involves both uptake and subsequent stability and cytoplasmic localization of extracellular proteins, some of the 39 hits also affected the transfer of RFP (Figure S3F; Table S1). We interpreted that to mean that the biology underlying the observed αSyn-RFP uptake effect for these hits is based on an effect on cell processes important for uptake and cytoplasmic localization of extracellular proteins.

Pharmacological validation supports the role of *SLC30A3*, *ADAMTS19*, *POLR2A*, *POLR2B*, and *WEE1* as regulators of αSyn transfer

We sought to confirm a subset of hits through an alternative method. We selected compounds that have been previously reported to target either the product of some of our hits directly or one of the pathways mediated by them. We transfected

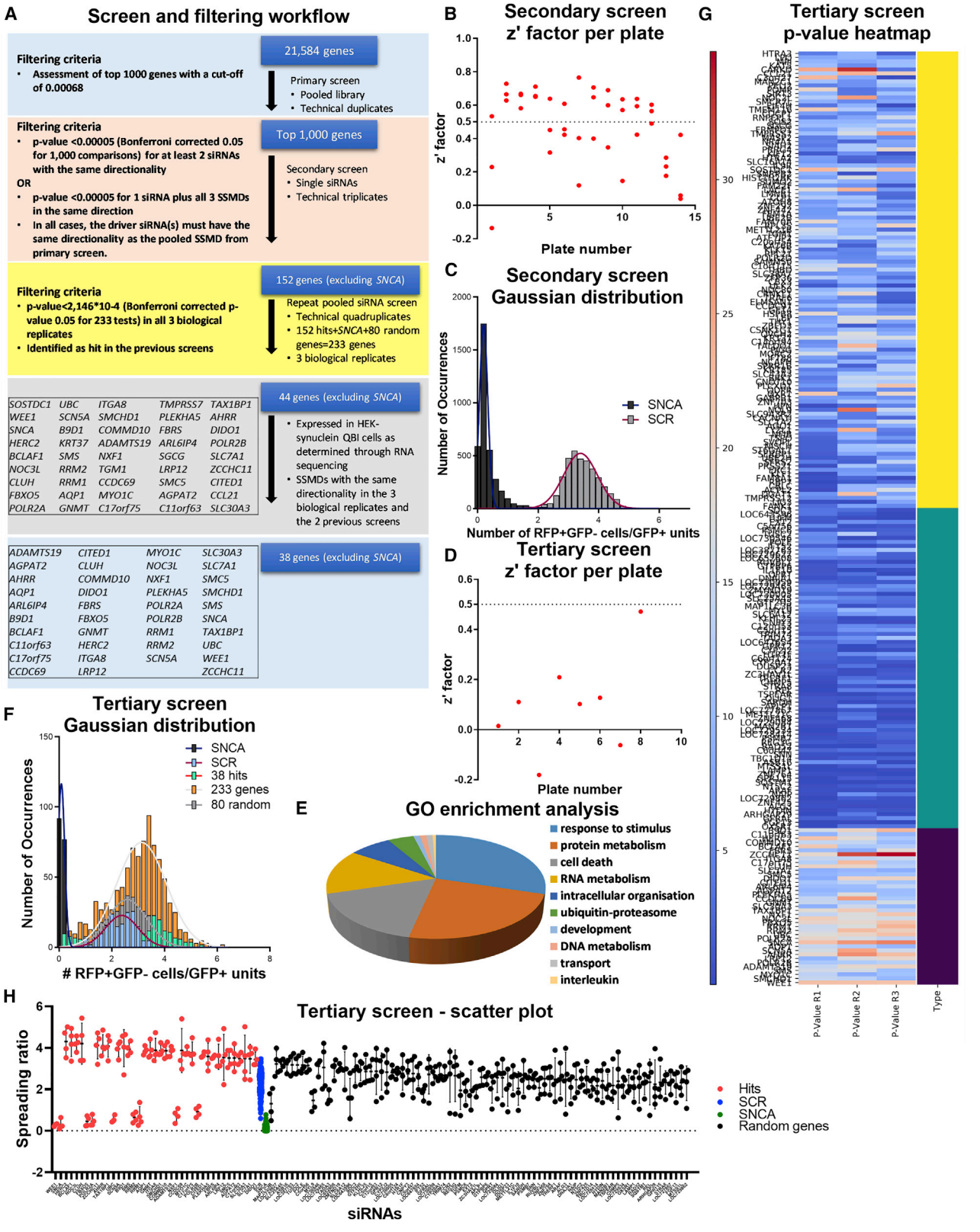

(legend on next page)

HEK-αSyn cells with the GFP-2A-αSyn-RFP construct and treated them with various concentrations of those compounds.

The zinc chelator *N*,*N*,*N*′,*N*′-Tetrakis(2-pyridylmethyl)ethylenediamine, treatment analogous to silencing *ADAMTS19* (a zinc-dependent metalloproteinase) and *SLC30A3* (a protein that mediates accumulation of zinc in synaptic vesicles), showed a significant dose-dependent effect, with the highest concentrations resulting in an increased transfer of αSyn (Figures 4A, 4D, and S4B). The directionality of this effect is consistent with that seen during the high-throughput imaging-based screens, in which silencing of those genes is associated with an increased transfer of αSyn.

α-Amanitin, which is a selective inhibitor of polymerase II and III, the protein product of *POLR2A* and *POLR2B*, showed a dose-dependent effect, with higher doses significantly reducing the transfer of αSyn (Figures 4B, 4E, and S4B). The directionality of this effect was consistent with what was seen in the imaging-based screen, in which silencing of *POLR2A* and *POLR2B* reduced αSyn transfer.

An indolylmethylene-2-indolinone derivative that acts as a Cdk1/cyclin B inhibitor by binding to the ATP pocket on the Cdk1 active site was also assessed. We expected that treatment with this compound would have the opposite effect of *WEE1* silencing, given that WEE1 is an inhibitor of Cdk1 (Den Haese et al., 1995). Indeed, treatment with the Cdk1 inhibitor showed a dose-dependent effect, with higher concentrations increasing the transfer of αSyn (Figures 4C, 4F, and S4B), whereas silencing of *WEE1* had an opposite effect.

As a control experiment, we assessed the dose-response effect of various concentrations of DMSO and ethanol (vehicle-only controls) on the transfer of αSyn. The transfer ratio was similar among all concentrations assessed (Figure S4A).

Assessment of the lysosomal-autophagy axis, mitochondrial mass, and cell cycle progression suggests links of the 38 hits with key functions related to the homeostasis of αSyn

We looked for additional evidence supporting the role of our 38 hits in the regulation of αSyn transfer. We optimized assays to assess the mitochondrial mass, the lysosomal-autophagy axis, and the cell-cycle progression, functions that have been shown to have a crucial role in the homeostasis of αSyn (Kara et al., 2013; Ludtmann et al., 2016, 2018; Ludtmann and Abramov, 2018; Wang et al., 2019).

LysoTracker is a dye that has been found to localize to the lysosomes and can therefore be used to indirectly measure lysosomal mass. MitoTracker is used to assess the mitochondrial mass; cells with reduced mitochondrial mass fluoresce less intensely when stained with MitoTracker. The cell-cycle assay is used for quantification of the proportion of cells that are in each stage of the cell cycle (Eddaoudi et al., 2018).

We generated dose-response curves for each of the dyes used in those experiments to confirm that the selected concentration was within the linear range (Figures 5A–5C). The subcellular distribution of the LysoTracker and MitoTracker dyes was assessed through imaging (Figure 5D). Several compounds were used as positive and negative controls Figures 5E and 5F). Those results were confirmed by using other colors of the same dyes (LysoTracker, blue; MitoTracker, far red) (Figures S5A–S5C).

The LysoTracker and cell-cycle assays were successfully miniaturized into a 96-well format (Figures 5G and 5H) and applied after transfection of HEK-αSyn cells with siRNAs against the 38 hits, *SNCA*, or 18 random genes. Although none of the samples reached statistical significance, the top 5 genes increasing LysoTracker and MitoTracker fluorescence upon silencing were hits from the high-throughput screening (HTS) (Figures 5I and 5J).

For the cell-cycle assay, the percentage of the cells in each phase of the cell cycle was quantified (G0/G1, S, and G2/M). Several of the hits had a tendency to increase cell proliferation, such as *WEE1*, as indicated by the fact that a decreased proportion of the cells were in the G0/G1 phase and an increased proportion in phases S and G2/M (Figures S5D–S5F). This is consistent with what is known about the function of *WEE1* as a regulator of cell-cycle progression through modulation of cdk1 (Den Haese et al., 1995). None of the hits significantly modified the RNA quantity within the cell, although there were hits whose silencing was associated with a sub-significant modification of RNA levels (Figure 5K). As the readouts were measured 3 days after transfection, the effect of the siRNAs at that time point was also quantified (Figures S5G and S5H).

Figure 3. Secondary and tertiary screens

(A) Step-wise process used during the high-throughput screens and follow-up analyses for gene filtering.

(B) Plot depicting the z′-factors of all plates included in the secondary screen. Only one plate had a negative z′-factor, and the average was 0.48.

(C) Histogram depicting all the positive and negative controls included in the secondary screen, showing a good separation between them.

(D) Plot showing the z′-factor per plate for one of the 3 tertiary screens.

(E) g:ProfileR analysis for the 38 screens confirmed after the tertiary screens.

(F) Histogram from 1 of the 3 tertiary screens showing the distribution of the positive and negative controls, 39 hits, 80 random genes, and all 233 genes included. There is a good separation between the positive and negative controls. The 39 hits cluster on either side of the bars depicting the random genes.

(H) Plot from 1 of 3 tertiary screens showing the separation between the final 38 hits and the random genes that were included. The hits show significantly higher or lower transfer ratios compared with that of the scrambled or αSyn controls, respectively, whereas the random genes are indistinguishable to the scrambled control.

(G) Heatmaps showing the p values for each of the 233 genes included in the tertiary screens. The 39 hits form a separate cluster that is identifiable through visual inspection. The 80 random genes are indistinguishable from the 114 hits from the primary screen that did not pass the cutoffs. Color code: purple, 39 hits; green, 114/152 filtered genes; and yellow, random genes.

The lists of genes depicted in the graphs in (G) and (H) are not easily readable because of their large number and are provided as an Excel sheet at the following repository: https://github.com/alecrimi/aSynuclein_siRNA_screen/blob/master/figure%203labellings.xlsx

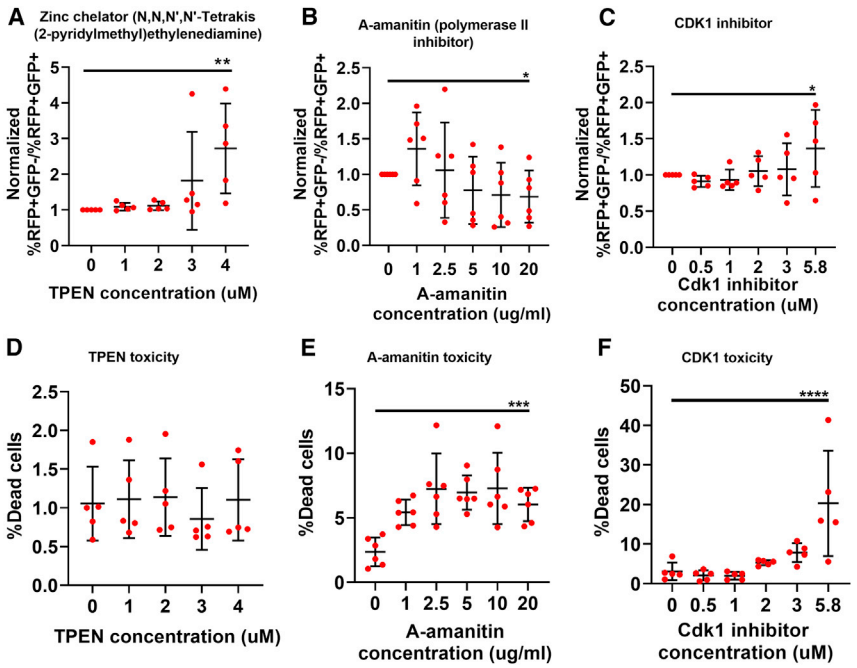

Figure 4. Replication of selected hits using pharmacological agents

(A) Plot showing the effect of the zinc chelator *N*,*N*,*N*′,*N*′-Tetrakis(2-pyridylmethyl)ethylenediamine (TPEN) on the cell-to-cell transfer of αSyn, as assessed through the GFP-2A-αSyn-RFP construct; 5 independent experiments were performed and were normalized to the negative control before meta-analysis. Statistical analysis was performed with one-way ANOVA with a test for trend. *p < 0.05 and >0.01, **p < 0.01 and >0.001, ***p < 0.001.

(B) Dose-response experiment for α-amanitin; 6 independent experiments were performed and were normalized to the negative control before meta-analysis. Statistical analysis was performed with one-way ANOVA with a test for trend. *p < 0.05 and >0.01.

(C) Dose-response experiment for the Cdk1 inhibitor; 5 independent experiments were performed and were normalized to the negative control before meta-analysis. Statistical analysis was done with one-way ANOVA with a test for trend. *p < 0.05 and >0.01.

(D) Toxicity associated with TPEN treatment, as assessed through the far-red live/dead staining. The experiment was repeated independently 5 times. Unnormalized values are shown.

(E) Toxicity measurement in the α-amanitin experiments using the far-red live/dead stain. Treatment with the compound was associated with a higher toxicity in comparison with the vehicle-only control, which, however, was on average less than 10%. The experiment was repeated independently 5 times. Unnormalized values are shown.

(F) Toxicity measurement in the cdk1-inhibitor experiments using the far-red live/dead stain. For the 4 lowest concentrations, the toxicity was similar to that of the vehicle-only control and was on average less than 10%. However, that increased to, on average, 20% for the highest concentration of the compound. The experiment was repeated independently 5 times. Unnormalized values are shown.

Weighted gene co-expression network analysis shows that most of the hits are included in the same networks as known PD genes

We used weighted gene co-expression network analysis (WGCNA) to assess whether our hits are related to known PD genes (Mendelian and genome-wide association study [GWAS] risk genes) by participating in the same genetic networks. We first assessed the ability of WGCNA to identify functional relationships between genes and their enrichment for cell-type-specific markers using known genes for PD and Alzheimer's disease (AD) as models. For PD, one module passed the p value threshold after correction for multiple testings. This module was within the substantia nigra, was significantly enriched for GO processes including catechol-containing biosynthetic processes and cell-to-cell signaling, and was enriched for dopaminergic neuron cell markers (Table S2). For AD, several significant modules within the hypothalamus, pituitary, hippocampus, nucleus accumbens, cortex, cerebellum, and caudate nucleus were found, all of which were enriched for GO functions related to the immune system and for microglial cell markers (Table S3).

We performed a similar analysis for our 38 hits. Assessment of the modules within all brain regions, after application of a cutoff nominal p value of 0.05, indicated several modules in which the hits cluster. Those modules were enriched for GO functions such as protein modification, regulation of gene expression, cytoskeletal organization, synaptic transmission, and organelle organization. Several of the modules were enriched for neuronal cell markers (Table S4). Finally, analysis of the Genotype-Tissue Expression (GTEx; version 6) dataset showed that 37/38 of the hits were expressed in human brain.

We then assessed whether our genes were functionally related to known PD genes (Table S1). We co-clustered the 38 hits with the PD genes in all brain tissues available in the GTEx (version 6) dataset in modules with nominal $p < 0.05$. Using only hits (37 genes) and PD genes that are present in the network, we found that 78% of the hits were present within modules that included at least 1 known PD gene. We then modeled the null distribution of the percentage of genes overlapping with PD genes by generating 100,000 random simulations, each of which containing 37 genes. Based on the fraction of times that we saw a greater percentage of overlap of the random gene lists with the PD genes than the percentage of overlap observed for the 37 hits, an empirical p value was generated. We found that the co-clustering of hits with PD genes occurred more frequently than expected by random chance, with an empirical p value of 0.014 (Figure S6). The hits that are located in the same modules as PD Mendelian and risk genes are listed in Table S5.

Finally, we assessed whether the 38 hits had any cell-type-specific characteristics. For that purpose, we performed an expression-weighted cell-type analysis (EWCE) (Skene and Grant, 2016). The 38 genes were expressed more frequently than expected by chance in granule neurons of the dentate gyrus (false-detection rate [FDR]-adjusted p value = 0.045) (Figure 6). Given the lack of replicability in other neuronal cell types and

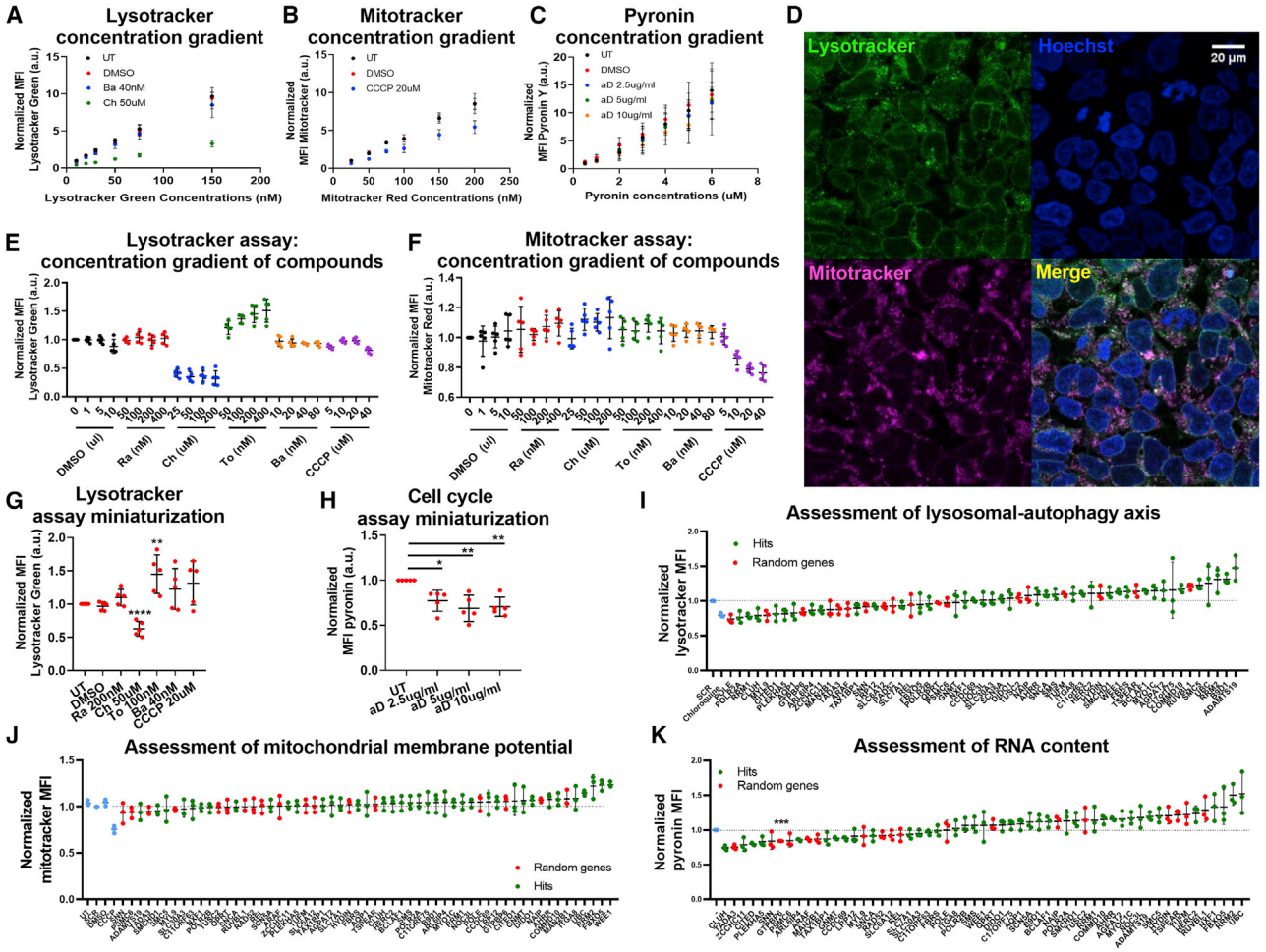

Figure 5. Assessment of the lysosomal-autophagy axis, mitochondrial mass, and cell cycle progression

(A) Dose-response experiment for the concentration of the LysoTracker dye in the LysoTracker experiment. The experiment was repeated 5 times independently, and the data were internally normalized to the lowest concentration of the dye before meta-analysis.

(B) Dose-response experiment for the concentration of the MitoTracker dye in the MitoTracker experiment. The experiment was repeated 5 times independently, and the data were internally normalized to the lowest concentration of the dye before meta-analysis.

(C) Dose-response experiment for the concentration of Pyronin Y in the cell-cycle experiment. The MFI of Pyronin Y increased in a linear way when the concentration of the dye increased. The positive control, actinomycin D, was clearly separated from the negative control (DMSO only), and the separation was largest at the greatest concentration. The experiment was repeated 5 times independently, and the data were internally normalized to the lowest concentration of the dye before meta-analysis.

(D) Confocal imaging of HEK-αSyn cells stained with the LysoTracker and MitoTracker dyes, depicting the subcellular distribution of those dyes. The concentration used for LysoTracker and MitoTracker was 150 nM. Scale bar, 20 μm.

(E) Dose-response experiment for the concentration of various compounds in the LysoTracker assay. The experiment was repeated 5 times independently, and the data were internally normalized to the lowest concentration of the negative control (DMSO only) before meta-analysis.

(F) Dose-response experiment for the concentration of various compounds in the MitoTracker assay. A good dose response was seen for CCCP but not for the other compounds. The experiment was repeated 5 times independently, and the data were internally normalized to the lowest concentration of the negative control (DMSO only) before meta-analysis.

(G) Miniaturized version of the LysoTracker assay in 96-well-plate format. The experiment was repeated 5 times independently, and the data were internally normalized to the untreated sample before meta-analysis. The statistical analysis was performed with one-way ANOVA with Tukey's correction for multiple testing. *$p < 0.05$ and >0.01, **$p < 0.01$ and >0.001, ***$p < 0.001$ and >0.0001, ****$p < 0.0001$.

(H) Miniaturized version of the cell-cycle assay in 96-well-plate format. A significant effect was seen for all concentrations of the positive control, actinomycin D. The experiment was repeated 5 times independently, and the data were internally normalized to the untreated sample before meta-analysis. The statistical analysis was performed with one-way ANOVA with Tukey's correction for multiple testing. *$p < 0.05$ and >0.01, **$p < 0.01$ and >0.001, ***$p < 0.001$ and >0.0001, ****$p < 0.0001$.

(I) The 57 different genes assayed for LysoTracker MFI (39 hits plus 18 random genes); 3 independent experiments were performed and normalized to the negative control before meta-analysis. Statistical analysis was performed using one-sample t tests, followed by the Bonferroni correction for multiple testings.

(legend continued on next page)

the limited availability of single-nuclear RNA sequencing data covering granule neurons of the dentate gyrus, which meant we could not validate the result, we interpret this result with caution.

Weighted protein-protein interaction network analysis confirms the functional relation between the 38 hits and known PD genes

As an additional way of confirming the functional connection between the 38 hits from the screen and the known PD genes, we performed weighted protein-protein interaction network analysis (WPPINA). We compared the overlap between Mendelian and risk PD genes with randomly generated gene lists. We drew the distribution curve of random overlaps between the random lists and the (real) PD Mendelian network (real node matches = 79 versus random nodes matches = 16) and between the random lists and the (real) risk network (real node matches = 132 versus random nodes matches = 28), which indicated that the real networks intersected more frequently than expected by random chance (Figures S7A and S7B). A visual representation of the overlap between those networks is depicted in Figures 7A and 7B. The intersection of the networks formed by the hits, the PD Mendelian, and the PD risk genes contained 50 genes (Figure 7C). GO enrichment analysis of those genes showed that the top 3 most-enriched processes were cell signaling (23.9%), cytoskeleton-mediated transport (22.7%), and cell death (18.2%) (Figure 7D).

Patients with PD do not carry an increased burden of rare variants within the 38 hits

We assessed whether the 38 hits contained risk variants that directly contribute to the causation of PD using the most recent International Parkinson Disease Genomics Consortium (IPDGC) GWAS summary statistics (Nalls et al., 2019). One gene, *ITGA8*, was a nominated candidate gene based on expression quantitative trait loci (eQTL) analysis (Nalls et al., 2019). Using a 500kb window, we found that 4 genes were included within the GWAS loci (*ARL6IP4*, *FBRS*, *POLR2A*, and *ITGA8*); however, this did not occur more frequently than expected by random chance. Burden analyses showed that the 38 genes were not enriched in rare PD-associated variants (Table S9).

FBXO5 regulates mitochondrial homeostasis and interacts with Parkin

One of the genes identified from the screen, *FBXO5*, belongs to the Fbxs family, as does *FBXO7*, a gene in which mutations cause a rare form of complex parkinsonism (Di Fonzo et al., 2009; Paisán-Ruiz et al., 2010; Shojaee et al., 2008) and whose protein product participates in mitochondrial homeostasis (Burchell et al., 2013; Delgado-Camprubi et al., 2017). We, therefore, hypothesized that FBXO5 has similar properties and assessed its role in mitochondrial homeostasis. We used *SNCA* knockout (KO) as a comparator, given that mitochondrial homeostasis has already been extensively characterized in that context (Ludtmann et al., 2016, 2018).

Although transmembrane mitochondrial potential ($\Delta\Psi m$) is generated mainly by the electron-transport chain and used as a proton-motive force for ATP synthesis, it is involved in most of the functions of the mitochondria, including calcium signaling and cell death (Abramov et al., 2017). Therefore, it can be considered as an indicator of mitochondrial "health." Using tetramethylrhodamine, methyl ester (TMRM) as a fluorescent indicator for $\Delta\Psi m$, we found that *SNCA* KO (deficiency) significantly reduced mitochondrial membrane potential (Figure S8A), which is in agreement with results from similar studies on αSyn deficiency (Ludtmann et al., 2016) or cells with triplication or overexpression of αSyn (Ludtmann et al., 2018; Reeve et al., 2015). Cells with FBXO5 deficiency or overexpression also had a lower mitochondrial membrane potential compared with the scrambled control (Figures S8A and S8B). Most (loss of function) parkinsonian mutations within genes, such as *PINK1*, *PARKIN*, *DJ-1*, and *LRRK2*, have a lower $\Delta\Psi m$ (Abramov et al., 2017; Ludtmann et al., 2019; Yao et al., 2011).

NADH is a substrate and donor of electrons for mitochondrial complex I. The respiratory activity of the cells and level of mitochondrial NADH can be assessed by measurements of NADH autofluorescence in live cells (Cheng et al., 2020). However, NADH cannot be separated from NADPH fluorescence. To separate the mitochondrial NADH signal, we used 1 μM of the mitochondrial uncoupler FCCP to maximize respiration and reduce NADH to minimum (taken as 0), followed by the addition of 1 mM of inhibitor of respiration NaCN, which blocks consumption of NADH in mitochondria and brings it to maximum (taken as 100) (Figures S8E–S8G). The difference between these values could be taken as the mitochondrial NADH pool, whereas the balance between NADH production and consumption (basal level) represents the redox level (Figure S8E). The redox level in *SNCA* KO cells was two times higher than that in the scrambled control (Figures S8E–S8D), suggesting inhibition of complex-I-dependent respiration. This has been previously shown for cells treated with oligomeric α-synuclein and for neurons with αSyn triplication (Ludtmann et al., 2018; Reeve et al., 2015). Interestingly, cells with *B9D1*, *ITGA8*, and *LRP12* KO, 3 genes identified as modifiers of αSyn transfer through our screen, also increased NADH redox levels, suggesting inhibition of respiration in these cells (Figure S8D). Importantly, cells with *FBXO5* KO had a significantly lower NADH redox level compared with the scrambled control, which, in combination with lower

(J) The 57 different genes assayed for MitoTracker MFI (39 hits plus 18 random genes). None of the genes assayed had a statistically significant effect on MitoTracker MFI, but the top-5 genes causing a hyperpolarization in the mitochondria were all hits; 3 independent experiments were performed and normalized to the negative control before meta-analysis. Statistical analysis was performed using one-sample t tests, followed by the Bonferroni correction for multiple testings. (K) The 57 different genes assayed for Pyronin Y MFI (39 hits plus 18 random genes). None of the hits assayed had a statistically significant effect on the MFI of Pyronin Y, but a random gene, *GTPBP6*, caused a significant reduction in the MFI; 3 independent experiments were performed and normalized to the negative control before meta-analysis. Statistical analysis was performed using one-sample t tests, followed by the Bonferroni correction for multiple testings. *$p < 0.05$ and >0.01, **$p < 0.01$ and >0.001, ***$p < 0.001$ and >0.0001, ****$p < 0.0001$. Abbreviations: Ch, chloroquine; To, torin; Ra, rapamycin; Ba, bafilomycin; CCCP, carbonyl cyanide m-chlorophenyl hydrazine; aD, actinomycin D

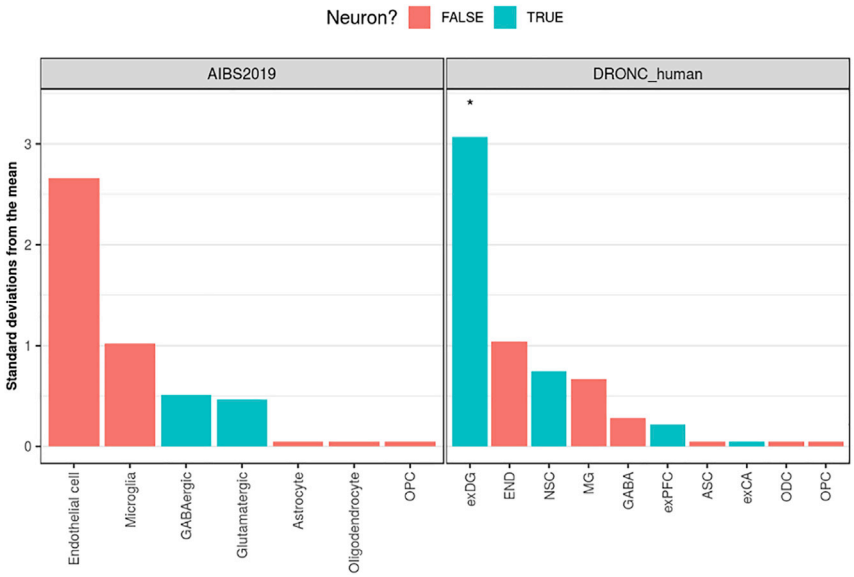

Figure 6. Expression-weighted cell-type analysis (EWCE)

Bootstrapping results from EWCE, using data from the Australia's International Business Survey 2019 (AIBS2019) study of the middle temporal gyrus or the *Drosophila* Nedd2-like caspase (DRONC) human study of the prefrontal cortex and hippocampus. Standard deviations from the mean denote the distance (in SD) of the target list from the mean of the bootstrapped samples. Asterisks used to denote results passing FDR < 0.05. Cell types on the x axis are colored by whether they are neuronally related. exPFC, glutamatergic neurons from the PFC; exCA1/3, pyramidal neurons from the Hip CA region; GABA, GABAergic interneurons; exDG, granule neurons from the Hip dentate gyrus region; ASC, astrocytes; NSC, neuronal stem cells; MG, microglia; ODC, oligodendrocytes; OPC, oligodendrocyte precursor cells; NSC, neuronal stem cells; SMC, smooth muscle cells; END, endothelial cells.

mitochondrial membrane potential in these cells (Figure S8A), suggests mitochondrial uncoupling (Figure S8D and S8F). The mitochondrial NADH pool (relative NADH concentration) was similar in scrambled, *SNCA*, and *B9D1* KO, suggesting that NADH production in the tricarboxylic acid cycle (TCA) remains unchanged (Figure S8C), whereas cells with *FBXO5*, *ITGA8*, and *LRP12* KO had a significantly lower mitochondrial NADH pool, which can suggest altered glucose metabolism or NAD consumption in the same way as in cells with *PINK1* or *FBXO7* deficiency (Delgado-Camprubi et al., 2017; Gandhi et al., 2009).

It has been shown that FBXO7 interacts with Parkin and PINK1 and participates in Parkin-mediated mitophagy. Using fluorescence resonance energy transfer (FRET) and fluorescence lifetime imaging microscopy (FLIM), we assessed whether FBXO5 can also interact with Parkin and whether it has the ability to form complexes. We found that there is a relatively weak interaction between FBXO5 and Parkin. FBXO5 was also found capable of self-associating (Figure S8H and S8I); the strength of that self-association was not altered after treatment with FCCP, oligomycin, rotenone, or CoCl2 (Figure S8I). Finally, we confirmed that the siRNAs against FBXO5 efficiently knock down their target and result in significant reduction in protein levels (Figure S8J).

DISCUSSION

We performed an siRNA screen to identify genes that regulate the cell-to-cell transfer of αSyn. We identified 38 genes that modulate this process, 9 of which decrease and 29 of which increase the transfer of αSyn upon silencing. Those genes were enriched in functions implicated in the homeostasis and intercellular spread of αSyn, such as cell-to-cell signaling, cytoskeletal-based transport, and waste disposal. Several of the identified genes have been previously linked to the pathogenesis of neurodegenerative diseases. *NFX1* has been identified through a CRISPR-Cas9 screen as a gene that reduces the levels of dipeptide repeat proteins (DRPs) by lowering the nuclear export of GGGGCCC-repeat-containing transcripts upon silencing (Cheng et al., 2019; Hautbergue et al., 2017). That gene was also identified through our screen as a reducer of αSyn spread upon silencing, presumably through lowering intracellular levels of αSyn, thereby having a consistent directionality of effect as reported in that screen.

Our screen also identified *FBXO5* as a hit that reduces αSyn transfer upon silencing. That gene belongs to the same family as *FBXO7*, a gene mutated in complex parkinsonisms (Di Fonzo et al., 2009; Paisán-Ruiz et al., 2010; Zhao et al., 2013) and which is involved in mitochondrial homeostasis and in the ubiquitin ligase complex called SCFs (SKP1-cullin-F-box) (Randle and Laman, 2016). TMRM experiments showed that FBXO5 induces mitochondrial depolarization upon silencing or overexpression, suggesting a role for that gene in mitochondrial homeostasis, similar to FBXO7 (Burchell et al., 2013). Similar effects have been previously observed for other genes mutated in parkinsonisms, including *PINK1*, *PARKIN*, *DJ-1*, and *LRRK2* (Abramov et al., 2017; Ludtmann et al., 2019; Yao et al., 2011). Finally, we found that FBXO5 interacts with Parkin, similarly to what has been previously shown for interaction between Parkin and FBXO7 (Burchell et al., 2013).

We found that *SLC30A3* and *ADAMTS19* increase the transfer of αSyn when silenced. Both those genes are implicated in the homeostasis of zinc. SLC30A3 has been implicated in the accumulation of zinc within the synaptic vesicles in mice (Cole et al., 1999), whereas ADAMTS19 is a member of the ADAMTS family of zinc-dependent proteases and has been implicated in the proteolysis of αSyn (Pampalakis et al., 2017). *ADAMTS4*, a gene belonging to the same family as *ADAMTS19*, has been identified as a candidate risk gene for AD through GWAS (Jansen et al., 2019). We have further shown that zinc chelation results in an increase of αSyn transfer, a directionality that is consistent with the effect seen when those 2 genes are silenced. There are several lines of evidence supporting a role for zinc in the pathogenesis of PD. It has been found that the parkinsonism gene *ATP13A2*

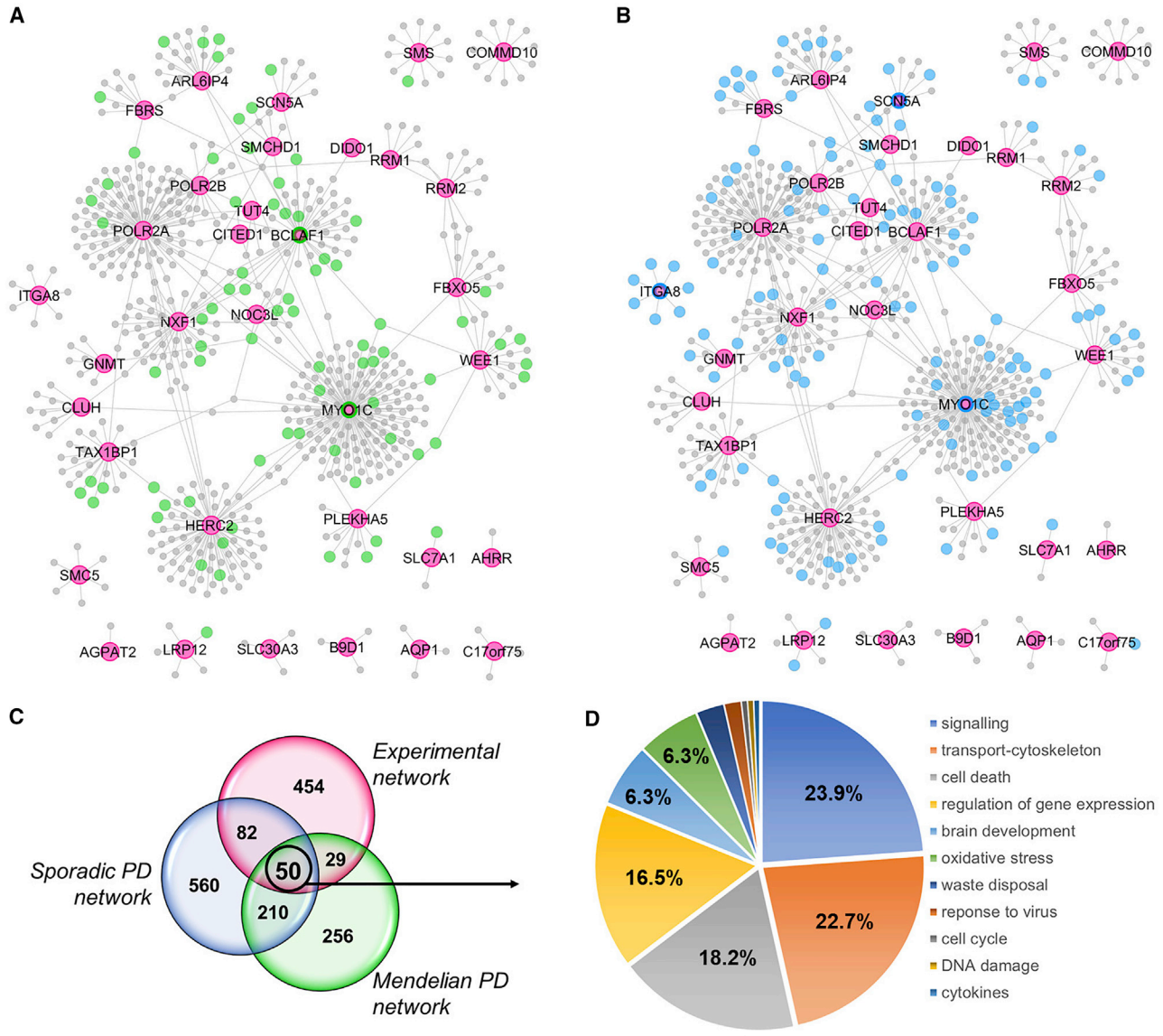

Figure 7. WPPINA confirms the functional relation between the 38 hits and known PD genes

(A) The 34 seeds from the "experiment" (Table S8) have been used as seeds for building the "Experimental protein-protein interactions network" or hits network. The network was built after downloading the (first layer) protein interactors of the seeds and by filtering for reproducibility of interactions. Pink nodes are the seeds of the experimental network, whereas green nodes are those that overlap across the experimental network and the protein-interaction network built around the PD Mendelian genes (Table S6).

(B) Pink nodes are the seeds of the experimental network, whereas blue nodes are those that overlap across the experimental network and the protein interaction network built around the risk (sporadic) PD genes (Table S7).

(C) Venn diagram detailing the overlaps across the nodes composing the experimental—Mendelian PD—sporadic PD networks.

(D) Functional enrichment (for Gene Ontology biological processes) performed with the 50 nodes that are communal across the 3 networks. Gene ontology terms are filtered and grouped into semantic classes by semantic similarity. General semantic classes have been excluded from the analysis (the entire enrichment is presented in Table S8).

encodes a zinc pump that facilitates transport of zinc into vesicles (Kong et al., 2014), similarly to *SLC30A3*. Reduced zinc levels in the serum and plasma have also been found in advanced forms of PD (Du et al., 2017).

LRP12, *ITGA8*, *TAX1BP1*, and *POLR2A*were also identified as hits from our screen. *LRP12* belongs to the same family as *LRP10*, a gene encoding a low-density lipoprotein-receptor-related protein, which carries risk variants in patients with PD (Quadri et al., 2018). A related gene, *LRP1*, has recently been found to regulate the uptake of tau (Rauch et al., 2020). *ITGA8* is a risk gene for PD, which was identified in the most recent PD GWAS meta-analysis (Nalls et al., 2019). In addition, Mendelian randomization-QTL analyses showed a significant association between decreased expression of *ITGA8* and PD risk (GTEx Consortium,

2013) (Nalls et al., 2019); concurrently, our data indicated that reduction in the expression levels of *ITGA8* results in an increase in the cell-to-cell transfer of αSyn. Finally, *ITGA8* downregulation has been found through an unbiased screen to increase the susceptibility of cells to infection with proteinase K-resistant PrP (PrP^{sc}) (Imberdis and Harris, 2014). *ITGA8* encodes alphα8 integrin, a heterodimeric transmembrane receptor that is involved in functions such as cell adhesion, cell signaling, and cytoskeletal organization (Humbert et al., 2014), functions that could all be related to the cell-to-cell transfer of αSyn. TAX1BP1 is an autophagy receptor with a role in xenophagy and in PINK1/Parkin-mediated mitophagy (Heo et al., 2015; Lazarou et al., 2015; Tumbarello et al., 2015; von Muhlinen et al., 2010; Wong and Holzbaur, 2014). It was recently shown that loss of TAX1BP1 results in accumulation of protein aggregates in the brain (Sarraf et al., 2020), which could be consistent with our results suggesting that reduction of TAX1BP1 increases cell transfer of αSyn. Finally, the *POLR2A* locus was recently identified as a putative genetic modifier of progression from PD to PD dementia (Liu et al., 2021).

Burden analyses did not identify an increased frequency of rare variants within the hits in patients with PD in comparison to healthy controls. However, it is possible that our hits are causal, but the current GWAS analysis methods and technologies were not sufficiently powered to detect such variants. GWAS have been designed to detect common variation related to complex diseases, and rare variants are difficult to impute with accuracy. In addition, structural variation is not captured in GWAS data.

The 38 genes that regulate the cell-to-cell transfer of αSyn participate in genetic and protein networks formed by Mendelian and risk PD genes. The fact that there is a genetic overlap between the phenomenon of αSyn spread and the causation of PD indicates that the role of αSyn transfer is a crucial part of the pathogenesis of the disease. Those observations support the validity of the ''prionoid'' hypothesis (Aguzzi et al., 2007; Aguzzi and Rajendran, 2009), in lieu of (or in combination with) alternative explanations for the progression of αSyn pathology, such as the selective-vulnerability hypothesis (Alegre-Abarrategui et al., 2019; Fu et al., 2018; Hardy, 2016).

In conclusion, this study has identified 38 genes that integrate within PD genetic networks and have a regulatory role on the cell-to-cell transfer of αSyn. Our work provides a framework for a gene-discovery strategy that could be applied to complex diseases when conventional genomic approaches are nearing limits of what is achievable.

Limitations

Our study had some technical limitations. We added an RFP tag to αSyn to enable its detection through imaging, without extra processing steps for antibody staining. Addition of a tag to αSyn modifies its ability to form aggregates (McLean et al., 2001), therefore possibly also modifying its ability to spread (Gustafsson et al., 2018). However, we have controlled for that limitation by including a negative control, GFP-2A-RFP. Conversely, our system has a significant advantage in that it studied the spread of αSyn produced endogenously from the donor, mammalian cells. Our study also did not make any assumptions about the aggregation status of the transferred species of αSyn, given that the nature of this species is still unclear (Cremades et al., 2012; Kurnik et al., 2018; Volles and Lansbury, 2003). This is an advantage over the commonly used system assessing the uptake of αSyn preformed fibrils (PFFs). Pandemic-related issues precluded the execution of some experiments requested by the reviewers, including replication on neuronal cultures using a different system with untagged αSyn, and validation through qPCR of a subset of siRNAs used for the screen.

STAR★METHODS

Detailed methods are provided in the online version of this paper and include the following:

- KEY RESOURCES TABLE
- RESOURCE AVAILABILITY
  - Lead contact
  - Materials availability
  - Data and code availability
- EXPERIMENTAL MODEL AND SUBJECT DETAILS
  - Tissue culture
- METHOD DETAILS
  - Molecular clonings
  - Flow cytometry assay to quantify the cell-to-cell transfer of αSyn
  - Flow cytometry assays to evaluate the mitochondrial mass and the lysosomal-autophagy axis
  - Flow cytometry assay to assess the cell cycle progression
  - Measurement of mitochondrial membrane potential
  - Measurement of NADH redox state
  - Fluorescence lifetime imaging microscopy (FLIM)
  - Forster resonance energy transfer (FRET)
  - High throughput screen (HTS)
  - Fluorescence-activated cell sorting (FACS)
  - Western blot
  - Reverse transcription quantitative PCR (RT-qPCR)
  - Weighted gene co-expression network analysis (WGCNA)
  - Expression weighted cell type enrichment (EWCE)
  - GWAS data and burden analyses
  - Weighted protein-protein interaction network interaction analysis (WPPINA)
  - Confocal imaging
  - RNA sequencing
- QUANTIFICATION AND STATISTICAL ANALYSIS

SUPPLEMENTAL INFORMATION

Supplemental information can be found online at https://doi.org/10.1016/j.celrep.2021.109189.

ACKNOWLEDGMENTS

Imaging was performed with support of the Center for Microscopy and Image Analysis, University of Zurich. Flow cytometry was performed with equipment of the flow cytometry facility, University of Zurich. RNA sequencing experiments and basic data analyses were performed at the functional genomics center Zurich (FGCZ). Flow cytometry was performed at the UCL Joint Great Ormond Street Institute of Child Health and Institute of Ophthalmology Flow

Cytometry Core Facility, supported by the Great Ormond Street Children's Charity (GOSHCC), grant reference U09822 (October 2007), UCL Capital Equipment Fund, School of Life and Medical Sciences (September 2012), and UK Research and Innovation, grant reference MR/L012758/1 (March 2014). FLIM imaging was performed at the UCL Confocal Imaging Facility, division of biosciences, which is funded by the UCL Capital Equipment Fund. E.K. is the recipient of an HFSP long-term fellowship (LT001044/2017), a Dr. Wilhelm Hurka Foundation project grant, and an EMBO, long-term fellowship (ATLF-815-2014, which is co-funded by the Marie Curie Actions of the European Commission [LTFCOFUND2013 and GA-2013-609409]). A.A. is the recipient of an Advanced Grant of the European Research Council (ERC 670958) and is supported by grants from the Swiss National Science Foundation (SNF 166943 and 179040) plus a Sinergia grant (183563), and a Distinguished Investigator Award of the NOMIS Foundation. J.H. is supported by the Medical Research Council (award number MR/N026004/1), the Wellcome Trust (award number 202903/Z/16/Z), the Dolby Family Fund, the National Institute for Health Research University College London Hospitals Biomedical Research Centre, and the BRCNIHR Biomedical Research Centre at University College London Hospitals NHS Foundation Trust and University College London. M.R. was supported through the award of a UK Medical Research Council Tenure Track Clinician Scientist Fellowship (MR/N008324/1). J.A.B. is supported through the Science and Technology Agency, Séneca Foundation, and CARM, Spain (research project 00007/COVI/20). R.H.R. was supported through the award of a Leonard Wolfson Doctoral Training Fellowship in Neurodegeneration. A.P.A.T. is supported by the Professor Dr. Max Cloëtta Foundation. C.M. and P.A.L. are supported by the Biomarkers Across Neurodegenerative Diseases Grant Program 2019, BAND3 (Michael J. Fox Foundation, Alzheimer's Association, Alzheimer's Research UK, and Weston Brain Institute [grant number 18063]). This work was supported by the UK Dementia Research Institute, which receives its funding from DRI Ltd, funded by the UK Medical Research Council, Alzheimer's Society, and Alzheimer's Research UK. This work was supported in part by the Intramural Research Programs of the National Institute of Neurological Disorders and Stroke (NINDS), the National Institute on Aging (NIA), and the National Institute of Environmental Health Sciences both part of the National Institutes of Health, Department of Health and Human Services; project numbers 1ZIA-NS003154, Z01-AG000949-02, and Z01-ES101986. The funders played no role in study design, data collection and analysis, decision to publish, or preparation of the manuscript. We would like to thank Gilles Kratzer (UZH Institute of mathematics) for expert advice on statistical analyses, Dr. Kelvin Luk (University of Pennsylvania) for providing us with vials of their HEK QBI WT synuclein cell line, Dr. Berend Snijder for allowing us access to his Opera Phenix for imaging a subset of plates, Dr. Giancarlo Russo for assistance with RNA sequencing analysis and data management, Dr. Christopher Thrasivoulou and Dr. Alan Greig for assistance with FLIM optimization, and Rita Moos and Jacqueline Wiedler for assistance with ordering consumables and grant administration.

AUTHOR CONTRIBUTIONS

Acquired funding, A.A., E.K., B.T.H., J.H., M.R., and P.A.L.; supervised study, A.A., B.T.H., J.H., M.R., P.A.L., J.A.B., E.K., and A.P.A.T.; performed clonings, E.K., Z.F., J.D.M., and A.W.; performed and optimized HTS imaging, E.K. and C.A.; optimized and performed wet-laboratory experiments for HTS, E.K.; performed and optimized confocal imaging, E.K.; printed siRNAs, E.K., M.C., M.E., M.A., D.H., A. Carrella, D.B.-S., L.M., D.P., and A.W.; analyzed GWAS data, S.B.-C. and C.B.; analyzed gene expression data, J.A.B., E.K., K.D., R.H.R., M.R., and S.G.-R.; analyzed protein-protein network interaction data, C.M. and P.A.L.; performed flow cytometry, E.K. and A.W.; performed FACS, M.L., V.L., E.K., and A.W.; performed western blot, E.K.; performed qPCR, E.K.; performed tissue culture, E.K., A.W., S.C.H., and J.D.M.; performed FRET and FLIM experiments, E.K.; performed mitochondrial experiments, A.Y.A. and E.K.; optimized and maintained robotics and provided critical advice on robotics usage, M.E.; analyzed wet-laboratory data, E.K., A. Crimi, A.W., and A. Chincisan; wrote code for analysis of HTS data, A. Crimi and A. Chincisan; RNA sequencing, A.D.M., D.H., M.A., and E.K.; wrote the manuscript, E.K. and A.A.; edited manuscript, all authors.

DECLARATION OF INTERESTS

B.T.H. has a family member who works at Novartis, and owns stock in Novartis; he serves on the scientific advisory board (SAB) of Dewpoint and owns stock; he serves on an SAB or is a consultant for Avrobio, AZTherapies, Biogen, Novartis, Cell Signaling, the U.S. Department of Justice, Takeda, Vigil, W20 Group, and Seer; and his laboratory is supported by sponsored research agreements with Abbvie and F-Prime and has research grants from the National Institutes of Health, Cure Alzheimer's Fund, Tau Consortium, and the JPB Foundation.

Received: December 21, 2019
Revised: February 8, 2021
Accepted: May 7, 2021
Published: June 8, 2021

REFERENCES

Abramov, A.Y., Berezhnov, A.V., Fedotova, E.I., Zinchenko, V.P., and Dolgacheva, L.P. (2017). Interaction of misfolded proteins and mitochondria in neurodegenerative disorders. Biochem. Soc. Trans. *45*, 1025–1033.

Aguzzi, A., and Rajendran, L. (2009). The transcellular spread of cytosolic amyloids, prions, and prionoids. Neuron *64*, 783–790.

Aguzzi, A., Heikenwalder, M., and Polymenidou, M. (2007). Insights into prion strains and neurotoxicity. Nat. Rev. Mol. Cell Biol. *8*, 552–561.

Alegre-Abarrategui, J., Brimblecombe, K.R., Roberts, R.F., Velentza-Almpani, E., Tilley, B.S., Bengoa-Vergniory, N., and Proukakis, C. (2019). Selective vulnerability in α-synucleinopathies. Acta Neuropathol. *138*, 681–704.

Bolger, A.M., Lohse, M., and Usadel, B. (2014). Trimmomatic: a flexible trimmer for Illumina sequence data. Bioinformatics *30*, 2114–2120.

Botía, J.A., Vandrovcova, J., Forabosco, P., Guelfi, S., D'Sa, K., Hardy, J., Lewis, C.M., Ryten, M., and Weale, M.E.; United Kingdom Brain Expression Consortium (2017). An additional k-means clustering step improves the biological features of WGCNA gene co-expression networks. BMC Syst. Biol. *11*, 47.

Braak, H., Del Tredici, K., Rüb, U., de Vos, R.A., Jansen Steur, E.N., and Braak, E. (2003). Staging of brain pathology related to sporadic Parkinson's disease. Neurobiol. Aging *24*, 197–211.

Burchell, V.S., Nelson, D.E., Sanchez-Martinez, A., Delgado-Camprubi, M., Ivatt, R.M., Pogson, J.H., Randle, S.J., Wray, S., Lewis, P.A., Houlden, H., et al. (2013). The Parkinson's disease-linked proteins Fbxo7 and Parkin interact to mediate mitophagy. Nat. Neurosci. *16*, 1257–1265.

Cahoy, J.D., Emery, B., Kaushal, A., Foo, L.C., Zamanian, J.L., Christopherson, K.S., Xing, Y., Lubischer, J.L., Krieg, P.A., Krupenko, S.A., et al. (2008). A transcriptome database for astrocytes, neurons, and oligodendrocytes: a new resource for understanding brain development and function. J. Neurosci. *28*, 264–278.

Campbell, R.E., Tour, O., Palmer, A.E., Steinbach, P.A., Baird, G.S., Zacharias, D.A., and Tsien, R.Y. (2002). A monomeric red fluorescent protein. Proc. Natl. Acad. Sci. USA *99*, 7877–7882.

Cheng, W., Wang, S., Zhang, Z., Morgens, D.W., Hayes, L.R., Lee, S., Portz, B., Xie, Y., Nguyen, B.V., Haney, M.S., et al. (2019). CRISPR-Cas9 Screens Identify the RNA Helicase DDX3X as a Repressor of C9ORF72 (GGGGCC)n Repeat-Associated Non-AUG Translation. Neuron *104*, 885–898.e8.

Cheng, X., Vinokurov, A.Y., Zherebtsov, E.A., Stelmashchuk, O.A., Angelova, P.R., Esteras, N., and Abramov, A.Y. (2020). Variability of mitochondrial energy balance across brain regions. J. Neurochem. Published online November 15, 2020. https://doi.org/10.1111/jnc.15239.

Chikte, S., Panchal, N., and Warnes, G. (2014). Use of LysoTracker dyes: a flow cytometric study of autophagy. Cytometry A *85*, 169–178.

Cole, T.B., Wenzel, H.J., Kafer, K.E., Schwartzkroin, P.A., and Palmiter, R.D. (1999). Elimination of zinc from synaptic vesicles in the intact mouse brain by disruption of the ZnT3 gene. Proc. Natl. Acad. Sci. USA *96*, 1716–1721.

GTEx Consortium (2013). The Genotype-Tissue Expression (GTEx) project. Nat. Genet. *45*, 580–585.

Cremades, N., Cohen, S.I., Deas, E., Abramov, A.Y., Chen, A.Y., Orte, A., Sandal, M., Clarke, R.W., Dunne, P., Aprile, F.A., et al. (2012). Direct observation of the interconversion of normal and toxic forms of α-synuclein. Cell *149*, 1048–1059.

de Calignon, A., Polydoro, M., Suárez-Calvet, M., William, C., Adamowicz, D.H., Kopeikina, K.J., Pitstick, R., Sahara, N., Ashe, K.H., Carlson, G.A., et al. (2012). Propagation of tau pathology in a model of early Alzheimer's disease. Neuron *73*, 685–697.

Delgado-Camprubi, M., Esteras, N., Soutar, M.P., Plun-Favreau, H., and Abramov, A.Y. (2017). Deficiency of Parkinson's disease-related gene Fbxo7 is associated with impaired mitochondrial metabolism by PARP activation. Cell Death Differ. *24*, 120–131.

Den Haese, G.J., Walworth, N., Carr, A.M., and Gould, K.L. (1995). The Wee1 protein kinase regulates T14 phosphorylation of fission yeast Cdc2. Mol. Biol. Cell *6*, 371–385.

Di Fonzo, A., Dekker, M.C., Montagna, P., Baruzzi, A., Yonova, E.H., Correia Guedes, L., Szczerbinska, A., Zhao, T., Dubbel-Hulsman, L.O., Wouters, C.H., et al. (2009). FBXO7 mutations cause autosomal recessive, early-onset parkinsonian-pyramidal syndrome. Neurology *72*, 240–245.

Dobin, A., Davis, C.A., Schlesinger, F., Drenkow, J., Zaleski, C., Jha, S., Batut, P., Chaisson, M., and Gingeras, T.R. (2013). STAR: ultrafast universal RNA-seq aligner. Bioinformatics *29*, 15–21.

Du, K., Liu, M.Y., Zhong, X., and Wei, M.J. (2017). Decreased circulating zinc levels in Parkinson's disease: a meta-analysis study. Sci. Rep. *7*, 3902.

Eddaoudi, A., Canning, S.L., and Kato, I. (2018). Flow cytometric detection of G0 in live cells by Hoechst 33342 and pyronin Y staining. Methods Mol. Biol. *1686*, 49–57.

Ferrari, R., Lovering, R.C., Hardy, J., Lewis, P.A., and Manzoni, C. (2017). Weighted protein interaction network analysis of frontotemporal dementia. J. Proteome Res. *16*, 999–1013.

Ferrari, R., Kia, D.A., Tomkins, J.E., Hardy, J., Wood, N.W., Lovering, R.C., Lewis, P.A., and Manzoni, C. (2018). Stratification of candidate genes for Parkinson's disease using weighted protein-protein interaction network analysis. BMC Genomics *19*, 452.

Fu, H., Hardy, J., and Duff, K.E. (2018). Selective vulnerability in neurodegenerative diseases. Nat. Neurosci. *21*, 1350–1358.

Gandhi, S., Wood-Kaczmar, A., Yao, Z., Plun-Favreau, H., Deas, E., Klupsch, K., Downward, J., Latchman, D.S., Tabrizi, S.J., Wood, N.W., et al. (2009). PINK1-associated Parkinson's disease is caused by neuronal vulnerability to calcium-induced cell death. Mol. Cell *33*, 627–638.

Gustafsson, G., Lööv, C., Persson, E., Lázaro, D.F., Takeda, S., Bergström, J., Erlandsson, A., Sehlin, D., Balaj, L., György, B., et al. (2018). Secretion and uptake of α-synuclein via extracellular vesicles in cultured cells. Cell. Mol. Neurobiol. *38*, 1539–1550.

Habib, N., Avraham-Davidi, I., Basu, A., Burks, T., Shekhar, K., Hofree, M., Choudhury, S.R., Aguet, F., Gelfand, E., Ardlie, K., et al. (2017). Massively parallel single-nucleus RNA-seq with DroNc-seq. Nat. Methods *14*, 955–958.

Hardy, J. (2005). Expression of normal sequence pathogenic proteins for neurodegenerative disease contributes to disease risk: 'permissive templating' as a general mechanism underlying neurodegeneration. Biochem. Soc. Trans. *33*, 578–581.

Hardy, J. (2016). Catastrophic cliffs: a partial suggestion for selective vulnerability in neurodegenerative diseases. Biochem. Soc. Trans. *44*, 659–661.

Hautbergue, G.M., Castelli, L.M., Ferraiuolo, L., Sanchez-Martinez, A., Cooper-Knock, J., Higginbottom, A., Lin, Y.H., Bauer, C.S., Dodd, J.E., Myszczynska, M.A., et al. (2017). SRSF1-dependent nuclear export inhibition of C9ORF72 repeat transcripts prevents neurodegeneration and associated motor deficits. Nat. Commun. *8*, 16063.

Hawrylycz, M.J., Lein, E.S., Guillozet-Bongaarts, A.L., Shen, E.H., Ng, L., Miller, J.A., van de Lagemaat, L.N., Smith, K.A., Ebbert, A., Riley, Z.L., et al. (2012). An anatomically comprehensive atlas of the adult human brain transcriptome. Nature *489*, 391–399.

Heo, J.M., Ordureau, A., Paulo, J.A., Rinehart, J., and Harper, J.W. (2015). The PINK1-PARKIN mitochondrial ubiquitylation pathway drives a program of OPTN/NDP52 recruitment and TBK1 activation to promote mitophagy. Mol. Cell *60*, 7–20.

Horn, M., Geisen, C., Cermak, L., Becker, B., Nakamura, S., Klein, C., Pagano, M., and Antebi, A. (2014). DRE-1/FBXO11-Dependent Degradation of BLMP-1/BLIMP-1 Governs C. elegans Developmental Timing and Maturation. Dev Cell *28*, 697–710.

Humbert, C., Silbermann, F., Morar, B., Parisot, M., Zarhrate, M., Masson, C., Tores, F., Blanchet, P., Perez, M.J., Petrov, Y., et al. (2014). Integrin alpha 8 recessive mutations are responsible for bilateral renal agenesis in humans. Am. J. Hum. Genet. *94*, 288–294.

Imberdis, T., and Harris, D.A. (2014). Prion permissive pathways: extracellular matrix genes control susceptibility to prion infection. EMBO J. *33*, 1506–1508.

Jansen, I.E., Savage, J.E., Watanabe, K., Bryois, J., Williams, D.M., Steinberg, S., Sealock, J., Karlsson, I.K., Hägg, S., Athanasiu, L., et al. (2019). Genome-wide meta-analysis identifies new loci and functional pathways influencing Alzheimer's disease risk. Nat. Genet. *51*, 404–413.

Kara, E., Hardy, J., and Houlden, H. (2013). The pallidopyramidal syndromes: nosology, aetiology and pathogenesis. Curr. Opin. Neurol. *26*, 381–394.

Kara, E., Marks, J.D., Fan, Z., Klickstein, J.A., Roe, A.D., Krogh, K.A., Wegmann, S., Maesako, M., Luo, C.C., Mylvaganam, R., et al. (2017). Isoform- and cell type-specific structure of apolipoprotein E lipoparticles as revealed by a novel Forster resonance energy transfer assay. J. Biol. Chem. *292*, 14720–14729.

Kara, E., Marks, J.D., Roe, A.D., Commins, C., Fan, Z., Calvo-Rodriguez, M., Wegmann, S., Hudry, E., and Hyman, B.T. (2018). A flow cytometry-based *in vitro* assay reveals that formation of apolipoprotein E (ApoE)-amyloid beta complexes depends on ApoE isoform and cell type. J. Biol. Chem. *293*, 13247–13256.

Kong, S.M., Chan, B.K., Park, J.S., Hill, K.J., Aitken, J.B., Cottle, L., Farghaian, H., Cole, A.R., Lay, P.A., Sue, C.M., and Cooper, A.A. (2014). Parkinson's disease-linked human PARK9/ATP13A2 maintains zinc homeostasis and promotes α-Synuclein externalization via exosomes. Hum. Mol. Genet. *23*, 2816–2833.

Kordower, J.H., Chu, Y., Hauser, R.A., Freeman, T.B., and Olanow, C.W. (2008). Lewy body-like pathology in long-term embryonic nigral transplants in Parkinson's disease. Nat. Med. *14*, 504–506.

Kurnik, M., Sahin, C., Andersen, C.B., Lorenzen, N., Giehm, L., Mohammad-Beigi, H., Jessen, C.M., Pedersen, J.S., Christiansen, G., Petersen, S.V., et al. (2018). Potent α-synuclein aggregation inhibitors, identified by high-throughput screening, mainly target the monomeric state. Cell Chem. Biol. *25*, 1389–1402.e9.

Langfelder, P., and Horvath, S. (2008). WGCNA: an R package for weighted correlation network analysis. BMC Bioinformatics *9*, 559. https://doi.org/10.1186/1471-2105-9-559.

Lawrence, M., Huber, W., Pagès, H., Aboyoun, P., Carlson, M., Gentleman, R., Morgan, M.T., and Carey, V.J. (2013). Software for computing and annotating genomic ranges. PLoS Comput. Biol. *9*, e1003118.

Lazarou, M., Sliter, D.A., Kane, L.A., Sarraf, S.A., Wang, C., Burman, J.L., Sideris, D.P., Fogel, A.I., and Youle, R.J. (2015). The ubiquitin kinase PINK1 recruits autophagy receptors to induce mitophagy. Nature *524*, 309–314.

Lein, E.S., Hawrylycz, M.J., Ao, N., Ayres, M., Bensinger, A., Bernard, A., Boe, A.F., Boguski, M.S., Brockway, K.S., Byrnes, E.J., et al. (2007). Genome-wide atlas of gene expression in the adult mouse brain. Nature *445*, 168–176.

Li, J.Y., Englund, E., Holton, J.L., Soulet, D., Hagell, P., Lees, A.J., Lashley, T., Quinn, N.P., Rehncrona, S., Björklund, A., et al. (2008). Lewy bodies in grafted neurons in subjects with Parkinson's disease suggest host-to-graft disease propagation. Nat. Med. *14*, 501–503.

Liu, G., Peng, J., Liao, Z., Locascio, J.J., Corvol, J.-C., Zhu, F., Dong, X., Maple-Grødem, J., Campbell, M.C., Elbaz, A., et al. (2021). Genome-wide survival study identifies a novel synaptic locus and polygenic score for cognitive

progression in Parkinson's disease. Nat Genet. https://doi.org/10.1038/s41588-021-00847-6.

Ludtmann, M.H.R., and Abramov, A.Y. (2018). Mitochondrial calcium imbalance in Parkinson's disease. Neurosci. Lett. *663*, 86–90.

Ludtmann, M.H., Angelova, P.R., Ninkina, N.N., Gandhi, S., Buchman, V.L., and Abramov, A.Y. (2016). Monomeric α-synuclein exerts a physiological role on brain ATP synthase. J. Neurosci. *36*, 10510–10521.

Ludtmann, M.H.R., Angelova, P.R., Horrocks, M.H., Choi, M.L., Rodrigues, M., Baev, A.Y., Berezhnov, A.V., Yao, Z., Little, D., Banushi, B., et al. (2018). α-synuclein oligomers interact with ATP synthase and open the permeability transition pore in Parkinson's disease. Nat. Commun. *9*, 2293.

Ludtmann, M.H.R., Kostic, M., Horne, A., Gandhi, S., Sekler, I., and Abramov, A.Y. (2019). LRRK2 deficiency induced mitochondrial Ca^{2+} efflux inhibition can be rescued by $Na^{+}/Ca^{2+}/Li^{+}$ exchanger upregulation. Cell Death Dis. *10*, 265.

Luk, K.C., Song, C., O'Brien, P., Stieber, A., Branch, J.R., Brunden, K.R., Trojanowski, J.Q., and Lee, V.M. (2009). Exogenous α-synuclein fibrils seed the formation of Lewy body-like intracellular inclusions in cultured cells. Proc. Natl. Acad. Sci. USA *106*, 20051–20056.

Luk, K.C., Kehm, V., Carroll, J., Zhang, B., O'Brien, P., Trojanowski, J.Q., and Lee, V.M. (2012). Pathological α-synuclein transmission initiates Parkinson-like neurodegeneration in nontransgenic mice. Science *338*, 949–953.

Luk, K.C., Covell, D.J., Kehm, V.M., Zhang, B., Song, I.Y., Byrne, M.D., Pitkin, R.M., Decker, S.C., Trojanowski, J.Q., and Lee, V.M. (2016). Molecular and biological compatibility with host α-synuclein influences fibril pathogenicity. Cell Rep. *16*, 3373–3387.

McLean, P.J., Kawamata, H., and Hyman, B.T. (2001). α-synuclein-enhanced green fluorescent protein fusion proteins form proteasome sensitive inclusions in primary neurons. Neuroscience *104*, 901–912.

Miller, J.A., Horvath, S., and Geschwind, D.H. (2010). Divergence of human and mouse brain transcriptome highlights Alzheimer disease pathways. Proc. Natl. Acad. Sci. USA *107*, 12698–12703.

Nalls, M.A., Blauwendraat, C., Vallerga, C.L., Heilbron, K., Bandres-Ciga, S., Chang, D., Tan, M., Kia, D.A., Noyce, A.J., Xue, A., et al.; 23andMe Research Team; System Genomics of Parkinson's Disease Consortium; International Parkinson's Disease Genomics Consortium (2019). Identification of novel risk loci, causal insights, and heritable risk for Parkinson's disease: a meta-analysis of genome-wide association studies. Lancet Neurol. *18*, 1091–1102.

Oldham, M.C., Konopka, G., Iwamoto, K., Langfelder, P., Kato, T., Horvath, S., and Geschwind, D.H. (2008). Functional organization of the transcriptome in human brain. Nat. Neurosci. *11*, 1271–1282.

Paisán-Ruiz, C., Guevara, R., Federoff, M., Hanagasi, H., Sina, F., Elahi, E., Schneider, S.A., Schwingenschuh, P., Bajaj, N., Emre, M., et al. (2010). Early-onset L-dopa-responsive parkinsonism with pyramidal signs due to ATP13A2, PLA2G6, FBXO7 and spatacsin mutations. Mov. Disord. *25*, 1791–1800.

Pampalakis, G., Sykioti, V.S., Ximerakis, M., Stefanakou-Kalakou, I., Melki, R., Vekrellis, K., and Sotiropoulou, G. (2017). KLK6 proteolysis is implicated in the turnover and uptake of extracellular α-synuclein species. Oncotarget *8*, 14502–14515.

Pease, D., Scheckel, C., Schaper, E., Eckhardt, V., Emmenegger, M., Xenarios, I., and Aguzzi, A. (2019). Genome-wide identification of microRNAs regulating the human prion protein. Brain Pathol. *29*, 232–244.

Quadri, M., Mandemakers, W., Grochowska, M.M., Masius, R., Geut, H., Fabrizio, E., Breedveld, G.J., Kuipers, D., Minneboo, M., Vergouw, L.J.M., et al.; International Parkinsonism Genetics Network (2018). LRP10 genetic variants in familial Parkinson's disease and dementia with Lewy bodies: a genome-wide linkage and sequencing study. Lancet Neurol. *17*, 597–608.

Randle, S.J., and Laman, H. (2016). F-box protein interactions with the hallmark pathways in cancer. Semin. Cancer Biol. *36*, 3–17.

Rauch, J.N., Luna, G., Guzman, E., Audouard, M., Challis, C., Sibih, Y.E., Leshuk, C., Hernandez, I., Wegmann, S., Hyman, B.T., et al. (2020). LRP1 is a master regulator of tau uptake and spread. Nature *580*, 381–385.

Reeve, A.K., Ludtmann, M.H., Angelova, P.R., Simcox, E.M., Horrocks, M.H., Klenerman, D., Gandhi, S., Turnbull, D.M., and Abramov, A.Y. (2015). Aggregated α-synuclein and complex I deficiency: exploration of their relationship in differentiated neurons. Cell Death Dis. *6*, e1820.

Reimand, J., Kull, M., Peterson, H., Hansen, J., and Vilo, J. (2007). g:Profiler–a web-based toolset for functional profiling of gene lists from large-scale experiments. Nucleic Acids Res *35*, W193–W200.

Rey, N.L., George, S., Steiner, J.A., Madaj, Z., Luk, K.C., Trojanowski, J.Q., Lee, V.M., and Brundin, P. (2018). Spread of aggregates after olfactory bulb injection of α-synuclein fibrils is associated with early neuronal loss and is reduced long term. Acta Neuropathol. *135*, 65–83.

Robinson, M.D., McCarthy, D.J., and Smyth, G.K. (2010). edgeR: a Bioconductor package for differential expression analysis of digital gene expression data. Bioinformatics *26*, 139–140.

Sarraf, S.A., Shah, H.V., Kanfer, G., Pickrell, A.M., Holtzclaw, L.A., Ward, M.E., and Youle, R.J. (2020). Loss of TAX1BP1-directed autophagy results in protein aggregate accumulation in the brain. Mol. Cell *80*, 779–795.e10.

Shojaee, S., Sina, F., Banihosseini, S.S., Kazemi, M.H., Kalhor, R., Shahidi, G.A., Fakhrai-Rad, H., Ronaghi, M., and Elahi, E. (2008). Genome-wide linkage analysis of a Parkinsonian-pyramidal syndrome pedigree by 500 K SNP arrays. Am. J. Hum. Genet. *82*, 1375–1384.

Skene, N.G., and Grant, S.G. (2016). Identification of vulnerable cell types in major brain disorders using single cell transcriptomes and expression weighted cell type enrichment. Front. Neurosci. *10*, 16.

Surmeier, D.J., Obeso, J.A., and Halliday, G.M. (2017). Parkinson's disease is not simply a prion disorder. J. Neurosci. *37*, 9799–9807.

Thakur, P., Breger, L.S., Lundblad, M., Wan, O.W., Mattsson, B., Luk, K.C., Lee, V.M.Y., Trojanowski, J.Q., and Björklund, A. (2017). Modeling Parkinson's disease pathology by combination of fibril seeds and α-synuclein overexpression in the rat brain. Proc. Natl. Acad. Sci. USA *114*, E8284–E8293.

Trempe, J.F., Sauvé, V., Grenier, K., Seirafi, M., Tang, M.Y., Ménade, M., Al-Abdul-Wahid, S., Krett, J., Wong, K., Kozlov, G., et al. (2013). Structure of parkin reveals mechanisms for ubiquitin ligase activation. Science *340*, 1451–1455.

Tumbarello, D.A., Manna, P.T., Allen, M., Bycroft, M., Arden, S.D., Kendrick-Jones, J., and Buss, F. (2015). The autophagy receptor TAX1BP1 and the molecular motor myosin VI are required for clearance of *Salmonella* Typhimurium by autophagy. PLoS Pathog. *11*, e1005174.

Volles, M.J., and Lansbury, P.T., Jr. (2003). Zeroing in on the pathogenic form of α-synuclein and its mechanism of neurotoxicity in Parkinson's disease. Biochemistry *42*, 7871–7878.

Volpicelli-Daley, L.A., Luk, K.C., Patel, T.P., Tanik, S.A., Riddle, D.M., Stieber, A., Meaney, D.F., Trojanowski, J.Q., and Lee, V.M. (2011). Exogenous α-synuclein fibrils induce Lewy body pathology leading to synaptic dysfunction and neuron death. Neuron *72*, 57–71.

von Muhlinen, N., Thurston, T., Ryzhakov, G., Bloor, S., and Randow, F. (2010). NDP52, a novel autophagy receptor for ubiquitin-decorated cytosolic bacteria. Autophagy *6*, 288–289.

Wang, X., Becker, K., Levine, N., Zhang, M., Lieberman, A.P., Moore, D.J., and Ma, J. (2019). Pathogenic α-synuclein aggregates preferentially bind to mitochondria and affect cellular respiration. Acta Neuropathol. Commun. *7*, 41.

Wegmann, S., Maury, E.A., Kirk, M.J., Saqran, L., Roe, A., DeVos, S.L., Nicholls, S., Fan, Z., Takeda, S., Cagsal-Getkin, O., et al. (2015). Removing endogenous tau does not prevent tau propagation yet reduces its neurotoxicity. EMBO J. *34*, 3028–3041.

Wegmann, S., Bennett, R.E., Delorme, L., Robbins, A.B., Hu, M., McKenzie, D., Kirk, M.J., Schiantarelli, J., Tunio, N., Amaral, A.C., et al. (2019). Experimental evidence for the age dependence of tau protein spread in the brain. Sci. Adv. *5*, eaaw6404.

Winden, K.D., Oldham, M.C., Mirnics, K., Ebert, P.J., Swan, C.H., Levitt, P., Rubenstein, J.L., Horvath, S., and Geschwind, D.H. (2009). The organization of the transcriptional network in specific neuronal classes. Mol. Syst. Biol. *5*, 291.

Wong, Y.C., and Holzbaur, E.L. (2014). Optineurin is an autophagy receptor for damaged mitochondria in parkin-mediated mitophagy that is disrupted by an ALS-linked mutation. Proc. Natl. Acad. Sci. USA *111*, E4439–E4448.

Xiao, B., Deng, X., Zhou, W., and Tan, E.K. (2016). Flow cytometry-based assessment of mitophagy using MitoTracker. Front. Cell. Neurosci. *10*, 76.

Yao, Z., Gandhi, S., Burchell, V.S., Plun-Favreau, H., Wood, N.W., and Abramov, A.Y. (2011). Cell metabolism affects selective vulnerability in PINK1-associated Parkinson's disease. J. Cell Sci. *124*, 4194–4202.

Zhan, X., Hu, Y., Li, B., Abecasis, G.R., and Liu, D.J. (2016). RVTESTS: an efficient and comprehensive tool for rare variant association analysis using sequence data. Bioinformatics *32*, 1423–1426.

Zhang, X.D. (2008). Novel analytic criteria and effective plate designs for quality control in genome-scale RNAi screens. J. Biomol. Screen. *13*, 363–377.

Zhao, T., Severijnen, L.A., van der Weiden, M., Zheng, P.P., Oostra, B.A., Hukema, R.K., Willemsen, R., Kros, J.M., and Bonifati, V. (2013). FBXO7 immunoreactivity in α-synuclein-containing inclusions in Parkinson disease and multiple system atrophy. J. Neuropathol. Exp. Neurol. *72*, 482–488.

STAR★METHODS

KEY RESOURCES TABLE

REAGENT or RESOURCE	SOURCE	IDENTIFIER
Antibodies		
mouse anti-actin antibody	Merck	Cat #MAB1501R; RRID:AB_2223041
HRP conjugated goat anti-mouse antibody	Jackson laboratories	Cat #115-035-003; RRID:AB_10015289
mouse anti-αSyn antibody	BD Bioscience	Cat #610786; RRID:AB_398107
Bacterial and virus strains		
DH5alpha chemically competent cells	ThermoFisher scientific	Cat #18258012
Chemicals, peptides, and recombinant proteins		
Hoechst 33342 dye	ThermoFisher	Cat #H3570
Alphα-amanitin	Merck AG	Cat #A2263-1MG
cdk1 inhibitor	Merck AG	Cat #217695-5MG
N,N,N′,N′-Tetrakis(2-pyridylmethyl)ethylenediamine	Merck AG	Cat #P4413-50MG
MitoTracker Red CMXRos dye	ThermoFisher	Cat #M7512
LysoTracker Green DND-2 dye	ThermoFisher	Cat #L7526
Chloroquine diphosphate	Sigma	Cat #C6628
Carbonyl cyanide m-chlorophenyl hydrazine (CCCP)	abcam	Cat #ab141229
Rapamycin	Sigma	Cat #R8781-200UL
Torin 1	Cayman chemicals	Cat #Cay10997-50
Bafilomycin A1	Sigma	Cat #B1793-10UG
LysoTracker Blue DND-22	ThermoFisher	Cat #L7525
MitoTracker Deep Red FM	Thermofisher	Cat #M22426
Actinomycin D	ThermoFisher	Cat #11805017
Pyronin Y	abcam	Cat #ab146350
Far red live dead	ThermoFisher scientific	Cat #L34974
Geneticin (G418)	ThermoFisher Scientific	Cat #10131035
Opti-MEM reduced serum medium (OMEM) with phenol	ThermoFisher Scientific	Cat # 31985047
Opti-MEM reduced serum medium without phenol	ThermoFisher Scientific	Cat #11058-21
Dulbecco's modified eagle medium (DMEM)	ThermoFisher Scientific	Cat #41965
Penicillin-streptomycin (PenStrep)	ThermoFisher Scientific	Cat #25300-054
Glutamax	GIBCO	Cat #35050-038
Fetal Bovine Serum (FBS)	Cat# SV30160.03HI	GE Healthcare Bio-Sciences Austria GmbH
Phosphate buffered saline (PBS) without Ca^{2+} and $Mg2^{+}$	ThermoFisher Scientific	Cat #14190-250
PDL (Poly-D-lysine hydrobromide, average mol wt 30,000-70,000)	ThermoFisher Scientific	Cat # P7280-5mg
Lipofectamine RNAiMAX Transfection Reagent	Invitrogen	#13778500
NuPage LDS sample buffer	ThermoFisher scientific	#NP0008
NuPAGE Sample Reducing Agent	ThermoFisher scientific	#NP0009
4-12% Bis-Tris gels	ThermoFisher scientific	#NP0321BOX
MES running buffer	ThermoFisher scientific	#NP0002
SureBlock	Lubioscience	#SB232010-50G
Crescendo HRP substrate	Merck	#WBLUR0100
Dimethyl sulfoxide (DMSO)	Sigma	#D8418-50ML

(*Continued on next page*)

Continued

REAGENT or RESOURCE	SOURCE	IDENTIFIER
Critical commercial assays		
Hispeed Plasmid Maxi Kit (10)	QIAGEN	Cat # 12662
Fast SYBR green Master mix	Applied Biosystems	Cat #4385612
Deposited data		
Code and datasets generated in this study	https://github.com/alecrimi/αSynuclein_siRNA_screen	N/A
Experimental models: cell lines		
HEK-αSyn cell line, Female origin	Dr. Kevin Luk (Luk et al., 2009)	N/A
HEK293T, Female origin	ATCC	N/A
SHSY5Y, Female origin	ATCC	N/A
HMC3, Male origin	ATCC	N/A
U251MG, Male origin	ATCC	N/A
GIMEN, Female origin	ATCC	N/A
Oligonucleotides		
primer targeting the αSyn-RFP transcript for qPCR (located within αSyn): 5'TGC CTT CTG AGG AAG GGT AT 3'	This paper	N/A
primer targeting the αSyn-RFP transcript for qPCR (located within RFP): 5'AAG CGC ATG AAC TCC TTG AT 3'	This paper	N/A
GAPDH housekeeping gene forward primer for qPCR: 5'AAG GTG AAG GTC GGA GTC AA 3'	This paper	N/A
GAPDH housekeeping gene reverse primer for qPCR: 5'AAT GAA GGG GTC ATT GAT GG 3'	This paper	
Forward primer for cloning of construct pAAV-CBA GFP-2αSyn: 5'AAAAAAGCTGAGCAGGATGTATTCATGAAAGG ACTTTCAAAGG 3'	This paper	N/A
Reverse primer for cloning of construct pAAV-CBA GFP-2A-αSyn: 5' AAAAAAGATATCCTGGGAGCAAAGATATTTCT TAGGC 3'	This paper	N/A
Forward primer for cloning of construct GFP-2A-αSyn-RFP (GFP-2α-αSyn portion): 5' AGTGTGGTGGAATTCTGCAGATGCCGCCACCATGGT GAGCAAGG 3'	This paper	N/A
Reverse primer for cloning of construct GFP-2A-αSyn (GFP-2α-αSyn portion): 5' GCCATAGGCGCTCCGATAAAGGCTTCAGGTTCG TAGTCTTGATAC 3'	This paper	N/A
Forward primer for cloning of construct GFP-2A-αSyn-RFP (RFP portion): 5' GCCTTTATCGGAGCGCCTATGGCCTCCTCCG AGGACG 3'	This paper	N/A
Reverse primer for cloning of construct GFP-2A-αSyn-RFP (RFP portion): 5' CCGCCACTGTGCTGGATTTAGGCGCCGGTGG AGTGG 3'	This paper	N/A
Forward primer for cloning the GFP-2A-RFP construct: 5'AAAAAGCTGAGCTT ATGGCCTCCTCCGAGGACG 3'	This paper	N/A

(*Continued on next page*)

Continued

REAGENT or RESOURCE	SOURCE	IDENTIFIER
Reverse primer for cloning the GFP-2A-RFP construct: 5' TTTTTGATATCTTAGGCGCCGGTGGAGTGG 3'	This paper	N/A
Forward primer for cloning of construct pcDNA3.1-FLAG-HA-RFP-FBXO5: 5' AAAAATCTAGAATGGCCTCCTCCGAGGA 3'	This paper	N/A
Reverse primer for cloning of construct pcDNA3.1-FLAG-HA-RFP-FBXO5: 5'AAAAATCTA GAATAGGCGCCGGTGGAGT 3'	This paper	N/A
Forward primer for cloning of construct pcDNA3.1-FLAG-HA-eGFP-FBXO5: 5'AAAAATCTAGAATGGTGAGCAAGG GCGA 3'	This paper	N/A
Forward primer for cloning of construct pcDNA3.1-FLAG-HA-eGFP-FBXO5: 5' AAAAATCTAGACTTGTACAGCTCGTCCATGCC 3'	This paper	N/A
siRNA Silencer Select Human Genome Wide Library	Silencer Select, Thermofisher	https://www.ncbi.nlm.nih.gov/pcsubstance?term=%2522Life%20Technologies,%20Applied%20Biosystems,%20Ambion%2522
Recombinant DNA		
pAAV-CBA GFP-2A-αSynuclein	Laboratory of Dr. Bradley Hyman	N/A
pcDNA3.1-GFP-2A-αSynuclein	This paper	N/A
pcDNA3.1-GFP-2A-αSynuclein-RFP	This paper	N/A
pcDNA3.1-GFP-2A-RFP	This paper	N/A
E3-RFP	Laboratory of Dr. Bradley Hyman	N/A
Software and algorithms		
ImageJ	https://imagej.net/Welcome	N/A
MATLAB	https://www.mathworks.com/products/matlab.html	N/A
Graphpad Prism version 8	https://www.graphpad.com/scientific-software/prism/	N/A
Applied Biosystems 7500 v2.04 operation software	Applied Biosystems	N/A
GTEx gene expression v6	https://gtexportal.org/home/	N/A
Cytoscape 2.8.2 software	https://cytoscape.org/	N/A
Plink	http://zzz.bwh.harvard.edu/plink/	N/A
STAR v2.5.1	Dobin et al., 2013	N/A
g:Profiler	http://biit.cs.ut.ee/gprofiler/	N/A
Flowing software 2	https://bioscience.fi/services/cell-imaging/flowing-software/	N/A
Echo CherryPick software	Labcyte	N/A
R	https://www.r-project.org/	N/A
Other		
IntAct	https://intact-systems.com/de/?gclid=EAIaIQobChMIitS0rOig5gIV1MqyCh01xwtVEAAYASAAEgIE7PD_BwE	N/A
BioGRID	https://thebiogrid.org/	N/A
InnateDB	https://www.innatedb.com/	N/A
PINOT analysis pipeline	http://www.reading.ac.uk/bioinf/PINOT/PINOT_form.html	N/A

(*Continued on next page*)

Continued

REAGENT or RESOURCE	SOURCE	IDENTIFIER
Allen Institute for Brain Science; Cell Diversity in the Human Cortex, published 2018-9	Hawrylycz et al., 2012; https://portal.brain-map.org/atlases-and-data/rnaseq#Previous_Human_Cortex	N/A
Expression Weighted Celltype Enrichment (EWCE)	Skene and Grant, 2016; https://github.com/NathanSkene/EWCE	N/A
CoExp Web application	https://rytenlab.com/coexp/Run/Catalogue	N/A
CoExpGTEx GitHub (suite of co-expression networks from the GTEx V6 gene expression data)	https://github.com/juanbot/CoExpGTEx	N/A

RESOURCE AVAILABILITY

Lead contact

Further information and requests for resources and reagents should be directed to and will be fulfilled by the lead contact, Prof. Adriano Aguzzi (Adriano.aguzzi@usz.ch).

Materials availability

Plasmids generated in this study can be shared by the authors upon request. Deposition to Addgene is in progress.

Data and code availability

The code and datasets generated during this study are available on Github https://github.com/alecrimi/αSynuclein_siRNA_screen

EXPERIMENTAL MODEL AND SUBJECT DETAILS

Tissue culture

A HEK QBI cell line stably overexpressing wild-type (WT) αSyn (hereafter referred to as HEK-αSyn line) was used in this study (Luk et al., 2009). This cell line was a kind gift from Dr Kelvin Luk (university of Pennsylvania). That cell line was cultured in the following medium: DMEM (#31053-036, ThermoFisher Scientific) + 10%FBS (Hyclone Heat inactivated, #SV30160.03HI, GE Healthcare Bio-Sciences Austria GmbH) + 1%glutamax (#35050-038, GIBCO) + 0.2mg/ml geneticin (#10131035, ThermoFisher Scientific).

The following cell lines were also used to assess the cell-to-cell transfer of αSyn: U251MG, GIMEN, SHSY5Y, HMC3, HEK293T. They were cultured in the following media: DMEM (#41965, ThermoFisher scientific) + 10%FBS + 1%glutamax + 1% penicillin-streptomycin (penstrep) (#25300-054, ThermoFisher scientific) (SHSY5Y, HEK293T), OMEM (31985047, ThermoFisher scientific) + 10% FBS + 1%glutamax + 1%penstrep (GIMEN, HMC3, U251MG).

All cell lines were grown at 37 degrees.

METHOD DETAILS

Molecular clonings

pAAV-CBA GFP-2A-αSyn: The pAAV-CBA-GFP-2A-tau construct (Wegmann et al., 2019; Wegmann et al., 2015) was used as a vector and was digested with EcoRV and BlpI. The insert was PCR amplified from the pcDNA3.1-αSynuclein construct using the following primers: forward: AAAAAAGCTGAGCAGGATGTATTCATGAAAGGACTTTCAAAGG, reverse: AAAAAAGATATCCTGGGA GCAAAGATATTTCTTAGGC. The vector and insert were ligated, transformed using DH5alpha chemically competent cells (#18258012, ThermoFisher), and the sequence of the miniprep product was confirmed through Sanger sequencing.

pcDNA3.1-GFP-2A-αSyn: The pcDNA3.1 vector was digested with HindIII and EcorV enzymes, followed by CIP treatment. The pAAV-CBA-GFP-2A-αSyn construct was digested with the same enzymes to isolate the GFP-2A-αSyn insert. Vector and insert were ligated, transformed using DH5a chemically competent cells, and the sequence of the miniprep product was confirmed through Sanger sequencing.

pcDNA3.1-GFP-2A-αSyn-RFP: The pcDNA3.1 backbone was digested with EcoRI, followed by CIP treatment. The GFP-2A-αSyn and RFP fragments were amplified through PCR using the following primers: GFP-2A-αSyn forward: AGTGTGGTGGAATTCTGCAGA TGCCGCCACCATGGTGAGCAAGG; GFP-2A-αSyn reverse: GCCATAGGCGCTCCGATAAAGGCTTCAGGTTCGTAGTCTTGATAC; mRFP forward: GCCTTTATCGGAGCGCCTATGGCCTCCTCCGAGGACG; mRFP reverse: CCGCCACTGTGCTGGATTTAGGCGCC

GGTGGAGTGG. Those fragments were ligated into the backbone through Gibson assembly, as per manufacturer instructions. Of note, monomeric RFP (mRFP) was used in this and in the two constructs described below (Campbell et al., 2002).

pcDNA3.1-GFP-2A-RFP: the pcDNA3.1-GFP-2A-αSyn vector was digested with BlpI and EcorV-HF to remove the αSyn fragment, followed by CIP treatment and gel purification. The mRFP insert was prepared through PCR amplification using pcDNA3.1-GFP-2A-αSyn-RFP as a template and the following primers: forward: AAAAAGCTGAGCTTATGGCCTCCTCCGAGGACG, reverse: TTTTTGATATCTTAGGCGCCGGTGGAGTGG. The digested vector and insert were ligated and transformed with DH5a chemically competent cells. The sequence of the miniprep products was confirmed through Sanger sequencing.

pcDNA3.1-FLAG-HA-RFP-FBXO5 and pcDNA3.1-FLAG-HA-eGFP-FBXO5: The pcDNA3.1-FLAG-HA-FBXO5 plasmid (addgene, #52509) was used as a vector and was digested with XbaI. The RFP insert was PCR amplified from the pcDNA3.1-E3-RFP construct (Kara et al., 2017; Kara et al., 2018) using the following primers: forward: AAAAATCTAGAATGGCCTCCTCCGAGGA, reverse: AAAAATCTAGAATAGGCGCCGGTGGAGT. The GFP insert was PCR amplified from the pcDNA3.1-GFP-2A-αSynuclein construct using the following primers: forward: AAAAATCTAGAATGGTGAGCAAGGGCGA, reverse: AAAAATCTAGACTTGTACAGCTCGTC CATGCC. The vector and insert were ligated, transformed using DH5alpha chemically competent cells and the sequence of the miniprep product was confirmed through Sanger sequencing.

pEGFP-parkin WT was a gift from Edward Fon (Addgene plasmid # 45875 ; http://addgene.org/45875 ; RRID:Addgene_45875) (Trempe et al., 2013). FLAG-HA-FbxO5-pcDNA3.1- was a gift from Adam Antebi (Addgene plasmid # 52509; http://addgene.org/52509 ; RRID:Addgene_52509)(Horn et al., 2014).

The cloning of the E3-RFP construct has been previously described (Kara et al., 2017, 2018).

All maxipreps were done using the Hispeed plasmid Maxi Kit (#12662, QIAGEN).

Flow cytometry assay to quantify the cell-to-cell transfer of αSyn

The HEK-αSyn cells were plated in 6 well plates at a density of 870 cells/ul. For the experiment where siRNAs were co-transfected with the constructs, the cells were plated in 24 well plates at a density of 870 cells/ul. 48h later, the cells were transfected with the GFP-2A-αSyn-RFP or the GFP-2A-RFP constructs, plus the siRNAs, as applicable. As single color controls for flow cytometry, the E3-RFP and GFP-2A-αSyn constructs were used. Before transfection, the medium in the 6 well plates was replaced with pure OMEM without phenol (#11058-21, ThermoFisher Scientific) by adding 1ml per well. The medium in the 24 well plates was replaced with the following medium, 440ul per well: pure OMEM without phenol plus 10%FBS plus 1%penstrep. For the transfection in 6 well plate format, 2 tubes were prepared, with the following amounts per well: One tube containing 150ul of pure OMEM without phenol plus 3ug of construct, and one tube containing 150ul of pure OMEM plus 9ul of RNAiMax (#13778500, Invitrogen). After 5min of incubation at room temperature, the contents of the tubes were mixed and 300ul of the mix was added per well. For the transfections in 24 well plate format, the following 2 tubes were prepared per well: One tube containing 30ul of pure OMEM plus 0.4ug of construct plus 0.5ul of stock siRNA solution with a concentration of 5uM, and a second tube containing 30ul of pure OMEM plus 1.8ul of RNAiMax. The final concentration of the siRNA in the tissue culture medium after addition to the cells was 5nM. After 5min of incubation at room temperature, the contents of the tubes were mixed and 60ul of the mix was added per well. 24h after transfection, the medium in the 6 well plates was replaced with the regular growth medium mentioned above. The medium in the 24 well plates was not replaced after transfection. On the 5th day after transfection, where applicable, Hoechst 33342 dye (#H3570, ThermoFisher) was added to PBS −/− (#14190-250, ThermoFisher Scientific) at a dilution of 1:2000. The medium was aspirated from the cells and was replaced with equal volume of the diluted Hoechst staining solution, followed by incubation at 37 degrees in the dark. The staining solution was then aspirated. At the same time, the medium from all wells that were not treated with Hoechst was also aspirated. The cells were washed with PBS −/−, trypsin was added and incubated at 37 degrees for 3min, regular growth medium (containing FBS) was added to inactivate trypsin, the cells were pipetted up and down to detach from the well and transferred to sterile eppendorf tubes, centrifuged at 1500rpm for 7min, and the supernatant was aspirated. At that point, the samples that required staining with far red live dead (#L34974, ThermoFisher scientific) were treated as follows: the stock live dead stain was reconstituted in 50ul of Dimethyl sulfoxide (DMSO) and diluted 1:1000 in PBS−/−. The pelleted cells were resuspended in 1000ul of that solution and incubated at room temperature, in the dark, for 30min. The samples were then centrifuged at 1500rpm for 7min. At that point, 500ul of 2% Paraformaldehyde (PFA) (in PBS−/−) was added to the cell pellet of all samples processed. The samples were stored at 4 degrees in the dark until analysis by flow cytometry.

Cells stained only with Hoechst or siRNA-cy5 or live dead far red were used as single color controls, where applicable. Of note, the far red live dead staining was never combined with the siRNA-Cy5 in the same sample because of the spectral overlap between the 2 dyes.

The siRNAs that were used were the following: a) siRNAs targeting the mRNA for αSyn, pooled into a single solution (*SNCA*): s13204, s13205, s13206 (#4427037, Silencer Select predesigned siRNAs, ThermoFisher), b) negative control (scrambled) siRNA: (#4390843, ThermoFisher), c) Cy5 tagged siRNA (siRNA-cy5): MISSION® siRNA Fluorescent Universal Negative Control #2, Cyanine 5 (#SIC006-5X1NMOL, Merck AG).

In the experiments where the effect of certain compounds on the cell-to-cell transfer of αSyn was assessed, 6 well plates were first coated with PDL (Poly-D-lysine hydrobromide, average mol wt 30,000-70,000, #P7280-5mg, ThermoFisher) before seeding the cells. 24h after transfection, the medium was changed to normal growing medium and cells were treated with the following compounds and concentrations: Alphα-amanitin (#A2263-1MG, Merck AG): 1, 2.5, 5, 10, 20ug/ml; cdk1 inhibitor (#217695-5MG, Merck AG): 0.5, 1, 2,

3, 5.8uM; N,N,N′,N′-Tetrakis(2-pyridylmethyl)ethylenediamine: 1, 2, 3, 4uM (#P4413-50MG, Merck AG). The appropriate vehicle-only controls were also included: Alphα-Amanitin: water; cdk1 inhibitor: DMSO; N,N,N′,N′-Tetrakis(2-pyridylmethyl)ethylenediamine: ethanol. On the 5th day after transfection, the cells were collected as described above. Hoechst and live dead stainings were also added.

Right before analysis through flow cytometry, the samples were filtered through a 35um cell strainer (#352235, Corning). The samples were analyzed on a BD Fortessa instrument (BD Biosciences). The following lasers and filters were used for the respective fluorophores: GFP: 488nm laser, 530/30nm emission filter; RFP: 561nm laser, 610/20nm emission filter; Hoechst: 405nm laser; 450/50nm emission filter; live dead far red: 640nm laser, 670/14nm emission filter. 100,000 events were recorded per sample. Compensations and voltages were adjusted based on the single color controls.

For the analysis of the flow cytometry data, single cells were gated using the FSC-A/FSC-H plot. The single color controls were used to set the gatings for the various fluorophores. The spreading ratio was calculated as follows: %RFP+GFP- cells/%RFP+GFP+ cells. Where applicable, the percentage of single cells that were positive for siRNA-Cy5 or Hoechst were also calculated. The number of cells that were dead was determined using the live dead histogram.

Flow cytometry assays to evaluate the mitochondrial mass and the lysosomal-autophagy axis

To quantify mitochondrial mass, we used the MitoTracker Red CMXRos dye (#M7512, ThermoFisher) and followed a similar procedure to a previously published experiment (Xiao et al., 2016). The stock vial contained 50ug of dye and was reconstituted in 94ul DMSO to a concentration of 1mM. The following concentrations were assayed in tissue culture and used for the dose-response experiment: 25, 50, 75, 100, 150, 200nM. 150nM were used for all other experiments.

To assess the lysosomal-autophagy axis, we used the LysoTracker Green DND-2 dye (#L7526, ThermoFisher) (Chikte et al., 2014). This dye is delivered by the company in reconstituted form, with a stock concentration of 1mM. The following concentrations were assayed in tissue culture and used for the dose-response experiment: 10, 20, 30, 50, 75, 150nM. 150nM were used for all other experiments.

Chloroquine diphosphate (#C6628, Sigma) was used as a positive control for the LysoTracker assay. The stock concentration was 25mM, in water. The following concentrations were assayed in tissue culture and used for the dose-response experiment: 25, 50, 100, 200uM. The concentration used in all other experiments was 50uM.

Carbonyl cyanide m-chlorophenyl hydrazine (CCCP) (#ab141229, abcam) was used as a positive control for the MitoTracker assay. The stock concentration was 10mM in DMSO. The following concentrations were assayed in tissue culture and used for the dose-response experiment: 5, 10, 20, 40uM. The concentration used in all other experiments was 20uM. As a vehicle-only control, DMSO was used.

Other compounds used in those 2 assays were the following:

Rapamycin (#R8781-200UL, Sigma): The stock concentration was 2.5mg/ml in DMSO. The following concentrations were assayed in tissue culture and used for the dose-response experiment: 50, 100, 200, 400nM. The concentration used in all other experiments was 200nM. As a vehicle-only control, DMSO was used.

Torin 1 (#Cay10997-50, Cayman chemicals): The stock concentration was 2.5mM in DMSO. The following concentrations were assayed in tissue culture and used for the dose-response experiment: 50, 100, 200, 400nM. The concentration used in all other experiments was 100nM. As a vehicle-only control, DMSO was used.

Bafilomycin A1 (#B1793-10UG, Sigma): The stock concentration was 4uM in DMSO. The following concentrations were assayed in tissue culture and used for the dose-response experiment: 10, 20, 40, 80nM. The concentration used in all other experiments was 40nM. As a vehicle-only control, DMSO was used.

For the assays in 24 well format, the HEK-αSyn cells were plated and 48h later transfected (if applicable), as described above. 3 days after transfection, they were incubated in the concentrations of Mitotracker or LysoTracker indicated above. The dyes were diluted in the following medium: pure OMEM without phenol+10%FBS+1% PenStrep. Right after, the cells were treated with the compounds at the concentrations previously indicated (as applicable). The cells were then incubated at 37 degrees for 3h. The cells were collected for analysis through flow cytometry, as previously described. The appropriate single color controls were also included.

For the assays in 96 well plate format (only applicable for the LysoTracker experiment), 96 well plates were coated with PDL. Those experiments were completed using reverse transfections. The siRNAs from the ThermoFisher Silencer Select library were printed using the ECHO555 acoustic dispenser (Labcyte). 100nl were printed per well for a final concentration of 5nM (that would occur after cell seeding and addition of transfection mix). The stock concentration of the library was 5mM, in distilled and sterile water. Each siRNA was printed in technical duplicates. 3 plates in total were used per batch of the experiment. Empty wells were left for addition of the positive and negative control treatments after cell seeding. The peripheral wells were used only for single color control samples because they are sensitive to temperature gradients and evaporations which could adversely affect the results of the siRNA experiments. The experiment was repeated independently 3 times. The plates were frozen until the reverse transfections took place.

The 96 well plates were defrosted in the fridge for 1h. A solution containing 19.6ul of pure OMEM and 0.36ul of RNAiMax per well was prepared and incubated for 5min at room temperature. 20ul were added per well. The plates were centrifuged at 2000 g for 1min and then incubated at room temperature for 20min. The cells were seeded at 870 cells/ul density and 80ul per well were added. 3 days later, the plates were prepared for analysis through flow cytometry. The dyes and compounds were added as described

above. 3h later, the medium was aspirated using the multichannel aspirator. 50ul of PBS−/− were added per well. This was aspirated and 10ul of trypsin were added per well, followed by 3min incubation at 37 degrees in the dark. 40ul of the following medium were added per well to inactivate the trypsin: pure OMEM without phenol+10%FBS+1%penstrep. 125ul of PBS−/−, followed by 25ul of 16%PFA were added per well, for a final volume of 200ul per well. The plates were analyzed using the high throughput accessory to the Fortessa instrument (BD Biosciences). The following parameters were used: Standard mode, 5x mix, 0.5 flow rate, 100ul mix volume, 500ul wash volume, 200 mix speed, 30ul sample volume. Each sample was recorded for 1min or 10,000 events, whichever was achieved first.

The following dyes were used for confirmatory purposes: LysoTracker Blue DND-22 (#L7525, ThermoFisher), MitoTracker Deep Red FM (#M22426, Thermofisher).

Flow cytometry assay to assess the cell cycle progression

A previously described method was followed for the cell cycle assay (Eddaoudi et al., 2018). Actinomycin D (#11805017, ThermoFisher), a transcription inhibitor, was included as a positive control. The stock concentration was 1mg/ml in DMSO. The following concentrations were assayed in tissue culture: 2.5, 5, 10ug/ml. 10ug/ml was used in all experiments. DMSO was used as a vehicle-only control. After addition of the positive control in predetermined wells, the cells were incubated with Hoechst dye diluted 1:2000 in PBS−/− for 45-75min (stock concentration was 10mg/ml). Pyronin Y (#ab146350, abcam) was then added at 20ug/well and incubated for another 45-75min (stock concentration was 2mg/ml in water).

For experiments completed in 24 well format, the cells were pelleted as previously described, but instead of being fixed in 2%PFA they were resuspended in $PBS^{-/-}$.

For experiments in 96 well format, the cells were prepared as follows: The medium was aspirated and 50ul of PBS−/− were added per well. The PBS was aspirated and 10ul of trypsin were added per well. After incubation at 37 degrees for 3min, 40ul of the following medium were added per well: pure OMEM without phenol+10%FBS+1% PenStrep. The cells were pipetted to facilitate detachment. 150ul of $PBS^{-/-}$ were added per well. In both versions of this experiment (24 well and 96 well), the cells were not fixed, because fixation affected the fluorescence properties of the dyes. The samples were analyzed using the high throughput accessory to the Fortessa instrument (BD Biosciences). The following parameters were used: Standard mode, 5x mix, 0.5 flow rate, 100ul mix volume, 500ul wash volume, 200 mix speed, 30ul sample volume. Each sample was recorded for 1min or 10,000 events, whichever was achieved first.

Measurement of mitochondrial membrane potential

Confocal images were obtained using Zeiss 710 CLSM microscope equipped with a META detection system and a 40 × oil immersion objective. Mitochondrial membrane potential was identified using the potential sensitive indicator tetramethylrhodamine (TMRM). Cells were loaded for 40 min at room temperature with 25 nM TMRM, excited at 565 nm and imaged with a 580 nm emission filter as previously described (Ludtmann et al., 2016). Measurements of TMRM fluorescence in cells were determined across z-stacks. Illumination intensity was kept to a minimum (at 0.1%–0.2% of the max laser output) to avoid phototoxicity and the pinhole set to give an optical slice of ~2 μm.

As a complementary approach, which would enable higher throughput, mitochondrial membrane potential was also measured through flow cytometry. Cells were transfected with siRNAs, as previously described. TMRM was added after 3 days at a concentration of 25nM and was incubated for 3h at 37 degrees in the dark. The cells were dissociated with trypsin and kept in suspension alive on ice until flow cytometry. Flow cytometry was performed on an LSRII instrument (BD biosciences). Excitation was done with a 488nm laser and a 757/26nm band pass emission filter was used. Approximately 100,000 cells were measured per condition and the MFI calculated.

Measurement of NADH redox state

NADH autofluorescence was measured using an epifluorescence inverted microscope equipped with a × 40 fluorite objective. Excitation light at a wavelength of 360nm was provided by a Xenon arc lamp, the beam passing through a monochromator (Cairn Research, Faversham, Kent, UK). Emitted fluorescence light was reflected through a 455nm long-pass filter to a cooled CCD camera (Retiga, QImaging, Surrey, BC, Canada) and digitised to 12 bit resolution. Imaging data were collected and analyzed using Andor iQ3 imaging software (Belfast, UK).

Fluorescence lifetime imaging microscopy (FLIM)

Fixed cells that were double transfected with single tagged RFP and GFP constructs, as well as singly transfected with GFP-FBXO5 as a negative control, were imaged on a Leica SP8 FALCON (FAst Lifetime CONtrast) microscope. A multiphoton laser was used to excite the GFP donor fluorophore with a two-photon excitation wavelength of 850nm. Data analysis was performed using the Leica Application Suite X (LAS X) software. The unquenched donor lifetime was determined by fitting a mono-exponential decay curve to the negative control (GFP-FBXO5). Single cells were used as the region of interest. Bi-exponential decay curves were fitted to the experimental samples by fixing the no-FRET lifetime, as determined through the negative control, and calculating the amplitude weighted lifetime through the software, which was then used to compare between experimental conditions. GFP-RFP fusion plasmid (Kara et al., 2017) was used as a positive control.

Forster resonance energy transfer (FRET)

FRET was performed through flow cytometry, as previously described (Kara et al., 2017). HEK-αSyn cells were fixed five days after transfection and were analyzed through flow cytometry. Cells were excited using a 488nm laser. GFP fluorescence was measured with a 530/30nm emission filter, and RFP with a 610/20nm filter. The FRET ratio was calculated by dividing the RFP to the GFP intensity per cell. Approximately 100,000 cells were measured per condition.

High throughput screen (HTS)

A commercially available library was used (Silencer Select, Thermofisher). This library contains 64,752 siRNAs (0.25nmol per siRNA) targeting 21,584 transcripts (i.e., 3 siRNAs per transcript) that were lyophilized in 384 well ECHO-qualified low dead volume (LDV) plates. The plates were reconstituted in distilled, sterile water to a concentration of 5mM. For the pooled version of the screen, 3ul of each individual siRNA targeting the same transcript were mixed, with a final concentration of 5mM and a final volume of 9ul.

The high throughput screen was completed as previously described (Pease et al., 2019). PDL-Coated CellCarrier-384 ultra 384 well plates were used as destination plates (#6057508, Perkin Elmer). 20ng of GFP-2A-αSyn-RFP construct that was reconstituted in distilled water were printed per well. Afterward, the library siRNAs were printed using the ECHO555 acoustic dispenser (Labcyte) that was controlled through the Echo Tempo software (Labcyte). 30nl of each siRNA (pooled or singlet, depending on the experiment) were dispensed per well, in technical duplicates spread over multiple plates. The distribution of the siRNAs in the destination plates was determined through a computer algorithm, with each technical duplicate printed on a different plate at a different position. Plates were printed in batches of 8. 44 positive (3 pooled siRNAs targeting *SNCA*) and 44 negative controls (scrambled siRNA) were included per plate, at a final concentration of 5nM. The controls were homogeneously distributed across plates, for quality control purposes. The peripheral wells in each plate (first and last row, first and last column) were excluded from analyses because they are sensitive to evaporation and temperature gradients and therefore the readout for the library siRNAs could have been adversely affected. A total of 166 destination plates were assayed in the primary, pooled screen. The plates were frozen until reverse transfections took place.

The plates were processed and analyzed in batches of 8. The plates were defrosted at 4 degrees for 1h before cell seeding. Reverse transfections were used. First, a mix containing the following reagents and volumes per well was prepared: 0.09ul of RNAiMax plus 4.91ul of pure OMEM without phenol. The mix was incubated at room temperature for 5min before adding 5ul per well. The plates were centrifuged at 2000 g for 1min and incubated at room temperature for 20min. The HEK-αSyn cells were trypsinized and seeded at a density of 870 cells/ul. 23ul of cells were added per well. The following medium was used: pure OMEM without phenol plus 10%FBS plus 1%penstrep. The plated cells were then kept in the incubator at 37 degrees for 5 days. To reduce the formation of temperature gradients, the plates were rotated manually in the incubator 1-2 times per day. They were rotated at 180 degrees across their longitudinal axis, along with change in position within the same shelf. The plates were spread out on the same shelf and not stacked.

On the 5th day after seeding, the plates were fixed. The medium was aspirated from the wells, 20ul of 2% PFA were added per well, the plates were incubated for 10-15min at room temperature in the dark, the PFA was aspirated, and 20ul of PBS −/− were added per well. The plates were wrapped in foil and stored at 4 degrees until imaging.

The GE IN Cell Analyzer 2500HS (GE Life Sciences) was used for imaging, with the following parameters: 10x objective (air), 2D deconvolution, 1x1 binning, BGOFR_1 polychroic beam splitter, software autofocus per channel, 10% laser power. The following lasers, emission filters and exposures were used: GFP: excitation 475/28nm, emission filter 511.5/23nm, exposure 0.06sec; RFP: excitation 542/27nm, emission 587.5/47nm, exposure 0.07sec. 2 images were acquired per well. Acquisition time per 384 well plate was less than 30min. A subset of plates (48) were imaged on the Opera Phenix (Perkin Elmer) using equivalent parameters.

During data analysis, all peripheral wells were excluded because they are more sensitive to evaporation and external insults. The metric that was used as a readout for the screen was the cell-to-cell transfer ratio of αSyn (number of $RFP^{+}GFP^{-}$ units/number of GFP+ units).

$$\frac{RFP^{+}\,GFP^{-}\,units}{GFP^{+}\,units} \qquad \text{(Equation 1)}$$

All analyses were done in MATLAB. First, the vignetting artifact, inherent to any microscopy experiment, was eliminated by global background subtraction where each image was divided pixel-by-pixel to the corresponding background. The background image was obtained using an operator size of 15 pixels. Further pre-processing included the use of a 2D median filter, automatic contrast adjustment and binarization. The binarization was obtained by thresholding the overall image for a fixed value (th = 0.1) for all images. This value has been optimized empirically. Once the images for both channels were computed, the difference between the red and green channel was calculated. The cell-to-cell transfer ratio was computed using that difference. A heatmap for each plate was also generated. The code used for data analysis and for the generation of the picklists is available on Github: αhttps://github.com/alecrimi/aSynuclein_siRNA_screen.

Two statistical metrics were used as quality control, the z'-prime factor and the strictly standardized mean difference (SSMD) (Zhang, 2008). Plates with a z'-factor below 0 were repeated, unless indicated otherwise in the results section of this manuscript.

$$SSMD = \frac{\overline{X}_P - \overline{X}_N}{\sqrt{s_P^2 + s_N}} \qquad \text{(Equation 2)}$$

$$Z' \text{ factor} = 1 - \frac{3 \times (\sigma_p + \sigma_n)}{|\mu_p - \mu_n|} \quad \text{(Equation 3)}$$

For each gene, the t test with the corresponding p value was computed and was used for ranking the hits, after Bonferroni correction for multiple testings. Other metrics that were calculated per gene and used mainly for visual representation of the data were the SSMD and log fold change. All those metrics were calculated relatively to the scrambled controls per batch of 8 384well plates.

Fluorescence-activated cell sorting (FACS)

Cells were plated in 35mm dishes at a seeding density of 870 cells/ul. 48h later, the cells were transfected with the GFP-2A-αSyn-RFP, E3-RFP or GFP-2A-αSyn constructs. 5 days later, the cells were washed with $PBS^{-/-}$ and trypsinized. Once the cells were detached, wells were pooled and subjected to centrifugation at 1500rpm for 7 min. Pellets were resuspended in FACS buffer (PBS, 2% FCS, 1 mM EDTA) and the samples proceeded to flow cytometry and sorting. Acquisition and sorting of cells was performed using a BD FACS Aria III 5L harnessing a 70 μm nozzle. The drop delay was performed using BD FACS Accudrop beads (BD Biosciences, #345249) according to the manufacturers' guidelines. Optical configurations were set as follows: a 488 nm Blue and a 561 nm YellowGreen laser were used for optimal excitation of GFP and RFP, respectively. The emission of GFP was recorded using a LP502 mirror in combination with a BP530/30 filter, whereas the RFP was recorded using a LP600 mirror in combination with a BP610/20 filter. Cells were gated for singlets on the FSC-A versus FSC-H plot and for debris exclusion on the FSC-A versus SSC-A plot. RFP+GFP- and RFP+GFP+ populations were determined on the plot for RFP versus GFP. Approximately 1,000,000 cells were collected per tube for the RFP+GFP+ population and 200,000 cells for the RFP+GFP- population.

Western blot

Cells were plated in 35mm dishes. Where applicable, they were transfected 48h after seeding with the GFP-2A-αSyn-RFP construct. 5 days later they were washed with PBS, trypsinized and pelleted with centrifugation at 1500rpm for 7min. The pellet was frozen until further usage. A pellet from a 35mm dish was lysated in 100ul of lysis buffer consisting of RIPA 1x (#9806S, Cell signaling) and cOmplete protease inhibitors 1x (#11697498001, Merck). For the FACS sorted cells, approximately 200,000 and 1,000,000 cells were lysated in 20ul of lysis buffer for the RFP+GFP- and the RFP+GFP+ populations, respectively. The protein concentration in each sample was measured with the BCA method (#23225, ThermoFisher scientific). A total of 20ug of protein were blotted per sample, after being diluted in 1x NuPage LDS sample buffer (#NP0008, ThermoFisher scientific) and 1x NuPAGE Sample Reducing Agent (#NP0009, ThermoFisher scientific) (final protein concentration 1ug/ul). The samples were run on 4%–12% Bis-Tris gels (#NP0321BOX, ThermoFisher scientific) at 120Volt at room temperature with 1x MES running buffer (#NP0002, ThermoFisher scientific). The gels were transferred onto PVDF membranes using the iBlot 2 dry blotting system. After blocking for 2h at room temperature in 5% SureBlock (#SB232010-50G, Lubioscience) in PBS, the membranes were incubated for 2h at room temperature in mouse anti-αSyn antibody, 1:1000 (#610786, BD Bioscience) in 1% SureBlock. Subsequently, the membranes were washed with PBS + 0.1% Tween and incubated with the secondary HRP conjugated goat anti-mouse antibody 1:12000 (#115-035-003, Jackson laboratories) for 1h at room temperature. After washing, the membranes were treated with Crescendo HRP substrate (#WBLUR0100, Merck) and imaged with the Fusion Solo 7S (witec ag). The membranes were also stained with a mouse anti-actin antibody for 1h at room temperature (#MAB1501R, Merck).

Reverse transcription quantitative PCR (RT-qPCR)

Cells were seeded in 35mm dishes and transfected as previously described. RNA was extracted from cells from a single 35mm dish using the miRNeasy Mini Kit (#217004, QIAGEN) and eluted in 30ul of ddH2O. DNAase I treatment (#79254, QIAGEN) was also included during RNA extraction. For FACS-isolated cells, RNA was extracted from 200,000 and from 1,000,000 cells for the RFP+GFP- and for the RFP+GFP+ populations, respectively. cDNA was generated using the High-Capacity cDNA Reverse Transcription Kit (ABI, # 4368814).

qPCR was performed following the relative standard curve method, as previously described (de Calignon et al., 2012). Briefly, five 10-fold serial dilutions of cDNA template from HEK-αSyn cells transiently transfected with the GFP-2A-αSyn-RFP construct were prepared for generation of the standard curve. 50ng of RNA reverse transcribed to cDNA were assayed per sample of interest. Each sample and each concentration of the standard curve were assayed in technical triplicates. No template controls were also included for each primer pair. A primer pair targeting the αSyn-RFP transcript (5′-TGC CTT CTG AGG AAG GGT AT-3′ within αSyn, 5′-AAG CGC ATG AAC TCC TTG AT-3′ within RFP) and the *GAPDH* housekeeping gene (5′-AAG GTG AAG GTC GGA GTC AA-3′, 5′-AAT GAA GGG GTC ATT GAT GG-3′) were used. For each sample, 5ul of cDNA were included in a reaction with 10ul of 2x Fast SYBR green master mix (#4385612, Applied Biosystems), 1ul of each of forward and reverse primers (3.3uM each) and 3ul of ddH2O. The samples were analyzed in 96 well plates on a 7500 Fast Real-Time PCR System (Applied Biosystems). Ct values were calculated using the 7500 v2.04 software (Applied Biosystems). Standard curves depicting the Ct values versus the log of the RNA input amount were generated for each of the genes. The RNA amount of each of the 2

transcripts was interpolated based on the standard curve for each of the samples assayed. *αSynRFP* expression was normalized to *GAPDH* expression for each sample, and the fold-difference in expression of *αSynRFP* in the RFP+GFP- sample was calculated relatively to the RFP+GFP+ (calibrator) sample.

Weighted gene co-expression network analysis (WGCNA)

WGCNA is based on the hypothesis that genes that are co-expressed are functionally related. Through WGCNA, genes are grouped in modules within each tissue studied, based on their expression patterns. Those modules can then be queried for the presence of particular genes, followed by the generation of a GO enrichment score and p value for the most enriched annotated functions. Enrichment for cell type-specific markers can also be assessed (Cahoy et al., 2008; Lein et al., 2007; Miller et al., 2010; Oldham et al., 2008; Winden et al., 2009; Botía et al., 2017). *SNCA* was excluded in all analyses to avoid introducing a PD-favorable bias.

In order to obtain co-expression models from brain tissue, we used GTEx gene expression V6. For all the 13 brain tissues available, we ran the same pipeline. For each tissue sample dataset, we selected only Ensembl genes expressed above 0.1 Reads per kilobase of transcript, per million mapped reads (RPKM) values at least in 80% of the corresponding samples. Then we corrected for batch effects with ComBat by using CENTER variable. Those residuals were normalized at sample and gene level and then the expression was further corrected for a number of SVA axes while controlling for age, sex and PMI covariates. The resulting gene expression values were regressed for PMI, age, sex and the surrogate variables detected by SVA. These residuals, along with the networks and annotations are accessible, for each tissue at the CoExpGTEx GitHub repository https://github.com/juanbot/CoExpGTEx. The co-expression networks are obtained with the WGCNA R package (Langfelder and Horvath, 2008) and an additional refinement step of the clusters, based on the k-means algorith implemented in the CoExpNets R package (Botía et al., 2017). We constructed a set of clusters from gene expression values based on correlation between genes across samples through building a gene expression adjacency matrix (with scale free topology). This was converted into a distance (Euclidean) based matrix that we used to create a dendrogram with the hclust package with default values for the corresponding method. Then we used k-means to refine the clusters obtained from the dendrogram. Network annotations are based on the gProfileR package (Reimand et al., 2007). All these models can be downloaded and used locally but they can also be accessed from a Web interface, the CoExp Web app https://rytenlab.com/coexp/Run/Catalog/.

For the proof of concept study where we sought to assess the ability of WGCNA to identify functional relationships between genes and their enrichment for cell type-specific markers, we used known Mendelian genes (cataloged in the Genomics England Panel App) and risk genes for PD (Nalls et al., 2019) (Table S1), and known risk genes for Alzheimer's disease (AD) (Jansen et al., 2019) and focused on modules within the brain.

Expression weighted cell type enrichment (EWCE)

EWCE (https://github.com/NathanSkene/EWCE) (Skene and Grant, 2016) was used to determine whether the 38 hits implicated in regulation of αSyn transfer have higher expression within particular brain-related cell types than would be expected by chance. This analysis tests whether the cell type specificity distribution of a certain gene list is greater in one cell type than would be expected if a random gene list of the same length that contained genes with a similar length and GC content was selected. As our input we used 1) the list of 38 hits (which excluded *SNCA*) and 2) specificity values calculated for level 1 cell types from two independent human single-nuclear RNA-sequencing (snRNA-seq) datasets. These datasets included 1) snRNA-seq data from the middle temporal gyrus (Allen Institute for Brain Science; Cell Diversity in the Human Cortex, published 2018; https://portal.brain-map.org/atlases-and-data/rnaseq/human-mtg-smart-seq) (Hawrylycz et al., 2012) and 2) massively parallel snRNA-seq with droplet technology (DroNc-seq) datasets from the prefrontal cortex and hippocampus (Habib et al., 2017). For the Allen Institute dataset, the cell-type specificity of each gene (i.e., proportion of total expression of a gene in one cell type compared to all others) was estimated using exonic read count values together with the 'generate.celltype.data' function of the EWCE package (specificity values and code used to generate these values available at: https://github.com/RHReynolds/MarkerGenes). Specificity values for the human DroNc-seq data had been previously published by Skene and Grant (2016). EWCE with the target list was then run with 100,000 bootstrap replicates, each of which was selected such that it had comparable transcript lengths and GC-content to the target list, thus controlling for these biases. Data are displayed as standard deviations from the mean, and any values < 0, which reflect a depletion of expression, are displayed as 0. P values were corrected for multiple testing using the Benjamini-Hochberg method over all level 1 cell types tested in both studies.

GWAS data and burden analyses

To investigate the role of the 38 identified genes and the effects of their genetic variation on the risk of PD, we utilized summary statistics from the latest International Parkinson's Disease Genomics Consortium (IPDGC) genome-wide association study (GWAS) consisting of 37.7K cases, 18.6K UK Biobank proxy-cases, and 1.4M controls, and including 7.8M SNPs (Nalls et al., 2019).

For gene-based burden analyses, IPDGC individual level data containing 21,478 cases and 24,388 controls was used (IPDGC dataset, excluding 23andMe cohort). The genotyping data underwent standard quality control and was imputed using the Haplotype Reference Consortium r1.1 2016 (http://www.haplotype-reference-consortium.org), under default settings with phasing using the EAGLE option, as previously described (Nalls et al., 2019). Imputed variants with more than 10% missing genotypes were excluded

and filtered for imputation quality (RSQ) > 0.8. Analyses were adjusted by sex, 10 principal components to account for population stratification, and dataset to account for possible chip bias. Since the variable age was missing for many patients, it was not included as a covariate in our analyses. The burden was computed in 2 different ways: a) within each gene individually, b) across WGCNA modules in which the hits clustered.

Gene-based burden analyses SKAT, SKAT-O, Madson Browing, Fp, Zeggini and CMC were performed by using RVTESTS (Zhan et al., 2016) to assess the cumulative effect of multiple variants at different minor allele frequency thresholds ($\leq$0.05, $\leq$ 0.03, $\leq$ 0.01) on the risk for PD according to default parameters.

Weighted protein-protein interaction network interaction analysis (WPPINA)

This analysis method was used to mine the literature for previously published protein-protein interactions and generate the networks that are formed by the proteins included in the input list. WWPNIA was completed as previously described (Ferrari et al., 2017, 2018). Briefly, the direct interactors (first layer nodes) of proteins of interest (seeds), as reported in the literature, were downloaded (June 2019) from the following repositories BioGrid, bhf-ucl, InnateDB, IntAct, MINT, UniProt, and MBInfo, as cataloged in the PSICQUIC platform. The pipeline for the download of interactors is freely available as an online tool (http://www.reading.ac.uk/bioinf/PINOT/PINOT_form.html). All interactors were filtered based on the number of publications in which they were reported and the number of different methods used, keeping interactions with a final score > 2. UBC was excluded from downstream analyses as it can bind to a large array of proteins targeted for degradation. Analyses were performed in R and networks were visualized with the Cytoscape 2.8.2 software.

The networks were generated separately for the 38 hits, the PD Mendelian genes and the PD GWAS risk genes. The network for the 38 hits (hits-network) included 34 seeds (4 hits were excluded as they did not show any interactor surviving our filtering step at the time of the analysis) plus the direct interactors of the seeds, for a total of 615 nodes. The PD Mendelian network included 18 seeds plus their direct interactors, for a total of 545 nodes. Finally, the PD risk gene network included 65 seeds and their direct interactors, total of 902 nodes. The overlap between a) the network of the hits and the PD Mendelian network, and b) the network of the hits and the PD risk gene network was then assessed by determining the communal nodes, which could be either seeds or direct interactors of the seeds. As a negative control, we generated 100,000 random gene lists, each comprising of 615 genes (to simulate the number of nodes in the real hits-network). We then calculated the overlap of these random lists with the real PD Mendelian and risk networks.

Gene Ontology (GO) terms enrichment analyses (June 2019) was performed in g:Profiler (http://biit.cs.ut.ee/gprofiler/).

Confocal imaging

Confocal imaging was performed on the Zeiss LSM 880 or 980 with Airyscan instruments. Cells were plated and transfected in 8 well glass bottom chamber slides (#055087, LabTek) and fixed in 2% PFA 5 days later for this experiment. Images were processed in ImageJ.

RNA sequencing

Cells of passage comparable to the one used for the HTS were analyzed through RNA sequencing to determine whether the genes detected as hits were indeed expressed.

The libraries were prepared following Illumina TruSeq stranded mRNA protocol. The quality of the initial RNA and the final libraries was determined using an Agilent Fragment Analyzer. The libraries were pooled equimolecularly and sequenced in an Illumina NovaSeq sequencer with a depth of around 20 Mio reads per sample.

FastQC was used for quality control of the reads. Sequencing adaptors were removed with Trimmomatic (Bolger et al., 2014) and reads were trimmed by 5 bases on the 3′ end. The TruSeq universal adaptor sequence was as follows: 5′ AATGATACGGCG ACCACCGAGATCTACACTCTTTCCCTACACGACGCTCTTCCGATCT. Reads that were at least 20bp long and had an average phred quality score over 10 were aligned to the human reference transcriptome using STAR v2.5.1 (Dobin et al., 2013) under default parameters for single end reads. The distribution of the reads across the isoforms transcribed was quantified with the R package GenomicRanges (Bioconductor Version 3.0) (Lawrence et al., 2013). Differentially expressed genes were identified with the R package EdgeR (Bioconductor Version 3.0) (Robinson et al., 2010). Genes with at least 10 raw counts in at least half of the samples were retained. The TMM normalized expression metric from EdgeR was used to determine if a gene was expressed or not.

QUANTIFICATION AND STATISTICAL ANALYSIS

All statistical analyses were performed in Graphpad Prism version 8.

For flow cytometry experiments, experiments were repeated 5-6 times independently, and each independent experiment contained 2 technical replicates per condition. The technical replicates were averaged and the independent experiments were collated for collective assessment of the data, after normalizing the data within each experiment to a common sample, usually the negative control or the first data point of a time course or dose response experiment, which was arbitrarily designated as 1 (Kara et al., 2017, 2018). In some cases where the absolute values were important (for example to assess cell viability), the data was not

normalized prior to collation of independent experiments. P values equal to or below 0.05 were considered significant. In experiments where more than one conditions were compared, the appropriate Bonferroni correction for multiple testing was used. The number of biological replicates conducted for each experiment, statistical test used, normalization process (if applicable), along with method for correction for multiple testing is indicated in the respective figure legend. In all scatterplots included in the paper, mean ± standard deviation is shown, and each dot represents the mean result from one independent experiment.

The analysis and quantification for the HTS, GWAS, WPPNIA, WGCNA, EWCE are included under the previous sections.